Microfluidic Devices for Cell Separation

David Inglis

A Dissertation

Presented to the Faculty

of Princeton University

in Candidacy for the Degree

of Doctor of Philosophy

Recommended for Acceptance

by the Department of

Electrical Engineering

September 2007

Abstract

The field of microfluidics is capable of poducing useful biological tools. Cell separation is one aspect of that larger biological tool, capable of isolating cells of interest from a complex background. This thesis describes two approaches for microfluidic cell separation, magnetic, and size-based. The first approach, magnetic separation, is achieved by selectively attaching magnetic beads to cells or cell populations, then altering their path using micro-fabricated ferromagnetic objects. This technique is primarily useful in selecting certain populations of cells that can be differentiated by the chemicals on their surfaces. This thesis describes the first demonstration of this type of microfluidic cell separation.

The second method, size-based cell separation, is achieved using a recently described method called deterministic lateral displacement, in which particles of different sizes follow one of two paths, through a micro-fabricated array of posts. This method can be used as a sort of continuously operable filter, separating large particles from small particles, or it can be used to measure the size of objects. This thesis describes numerous applications of the technique to the separation of blood components and the measurement of blood cells.

The two methods complement one another in that magnetic separation takes advantage of differences in surface chemical properties, while the size separation takes advantage of morphological properties.

Acknowledgements

Thank you very much Lisa, you taught me more than anyone. Thanks to my entire family, Mom and Dad, Robert, Nicole and Lorraine. Thanks to The Cousins, especially Cory Sutela for showing everyone how it could be done. Thanks to the aunts and uncles. Thanks to Princeton friends and to my oldest friend Adam.

Many thanks to Professors Jim Sturm and Bob Austin, and Dr. David Lawrence, and to their respective groups. Thanks to Dr. James White at the University of Minnesota for advice on experimental work with platelets. Thank you to my co-authors, John Davis, Robert Riehn, T.J. Ziezeulewicz, and espeically Keith Morton who saved me many trips to Cornell.

To my Nana Reta

Contents

Chapter 1

Introduction

1.1 Background and Motivation

The field of microfluidics has exploded in the 27 years since Andreas Manz [1] coined the term miniaturized total analysis system, now synonymous with micro total analysis system, μTAS. Many top research universities now have someone who specializes in the field, though interestingly that person could belong to any science or engineering department. Microfluidics refers to the science and engineering of fluids in micro or nano-scale structures. A basic microfluidic device is two layers, at least one usually being transparent, sandwiched together. Typically, one layer has tiny channels in it to carry the fluid, while the other layer seals the channels to make tubes. Somewhere there must also be vertical holes to allow for sample input and output and so that electrical or pressure connections can be made to drive the fluid.

The concept of miniaturized total analysis systems, or lab-on-a-chip, describes a conceptual device that performs many different physical, chemical and biological steps in a single device in a timely fashion. Despite years of research and much hype, such a device has never been mass produced. Some of the appeal for such a device draws on three pieces of technology and culture: science fiction, the engineering marvel that

is the computer, and MEMS, micro-electro mechanical systems.

In the fictional Star Trek universe, medical information is frequently gathered using a *tricorder*. It hums and it chirps as it scans, without touching, the patient. Within seconds the doctor would know what afflicts the patient. That we have no concept of what goes on inside the box doesn't matter. It is similar to the home computer, where most users have no comprehensive understanding of what's going on inside the box. We have faith in technology, and why not? History has taught that the fantastic can be achieved.

The modern computer is a fantastic piece of integrated and miniaturized machinery. The transistors that are the switches or logical operators on a microchip today are over 2000 times smaller than the first ones developed in late 1947 by Bardeen and Brattain. This, combined with decades of materials engineering, has allowed the switches to operate so fast that a thousand miles of code, written like this (01101001 01101100 01101111 01110110 01100101 01101100 01110111) can be processed in less than a second (almost 4 million miles per hour if the computer moved and the code didn't). Thanks also to decades of software engineering, user friendly input and output is effortlessly translated into binary code like that above. The lab on chip device is like a computer because it too has miniaturized components that perform different tasks integrated together to complete a single job.

MEMS devices are microfabricated machines that interact with their environments. They include microscopic motors, springs, gears, and levers, chemical and biological sensors and emitters. These micron-sized devices are, among other things, commonly used to measure acceleration in automotive safety systems like air bags. They are made using many of the same techniques and machines that make microelectronics, techniques like photolithography, thin metal and insulator coatings, and wet and dry etches.

Despite the fact that the overarching theme in nearly all microfluidics work is

the lab-on-a-chip or "micro total analysis system" concept, only a fraction of this literature describes complex integrated devices that perform many different tasks. Perhaps because the work of integrating many disparate processes is so hard, while demonstrating new individual capabilities of microfluidics is so exciting, not much integration has been done so far. Most of the work in the field of microfluidics, including this work, explores individual capabilities that may or may not, one day make it into a lab-on-a-chip.

The described work delineates two concepts within the microfluidics field. One addresses an attempt to perform biological experiments with single molecules, single pieces of DNA, RNA, proteins etc. Scientists are interested in these single entities because there are unexpectedly large variations in organisms or cells with the same genetics and similar environments [2]. And in order to better understand the link between the chemistry of organisms or cells and their behavior we must start by capturing one cell, not millions as typically used by biologists. Microfluidics, because of its size is a natural approach for working with a few cells and even single molecules.

The second concept is miniaturized point of care medical devices. In fact we already have these; home pregnancy tests and blood glucose meters are two examples. With microfluidics and the integration of laboratory processes onto small portable devices we can start to imagine a handheld blood meter that gives a complete blood analysis in minutes [3,4].

Both of the devices described above, a single cell analyzer and a handheld blood analyzer, must separate one type of cell from another. This dissertation will focus on two types of microfluidic cell separation devices, each of which has had an impact on the field of microfluidics.

Throughout this work, and in microfluidics work in general, the concept of low Reynolds number flow is important. The Reynolds number is often used by engineers to communicate whether a fluid is turbulent or not. The Reynolds number is the
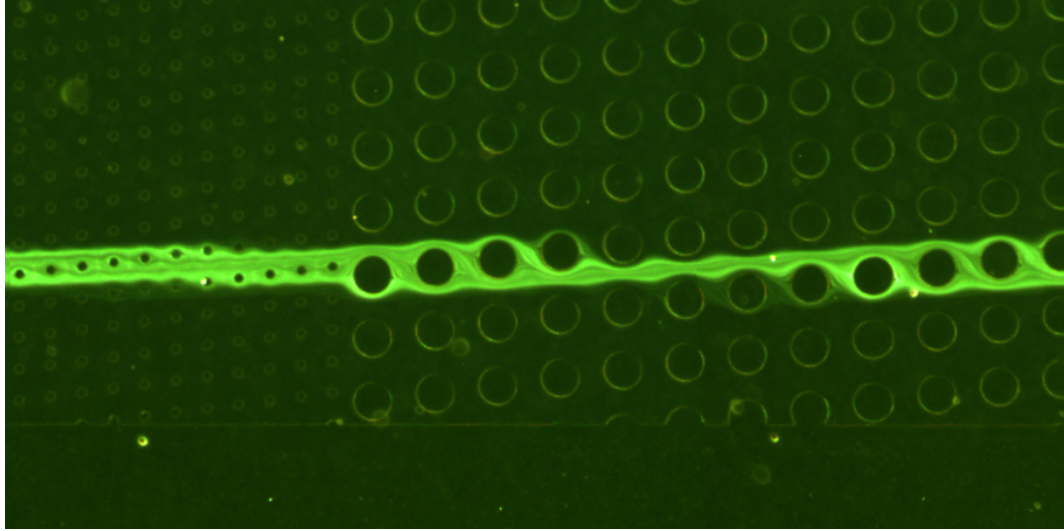
Figure 1.1: Micrograph of a stream of many 2.3 micron diameter fluorescent green beads flowing left to right though arrays of 13-and 54-micron-diameter posts

ratio of inertial forces to viscous forces and can be written,

$$\vec{R}_e = \frac{\rho v L}{\mu}, \tag{1.1}$$

where ρ is the fluid density, v is average fluid velocity, L is characteristic length scale such as a pipe diameter, and μ is the fluid viscosity. For a round pipe, the fluid will be flowing turbulently when the Reynolds number is greater than 2300. Turbulent flow involves rapid changes in pressure and velocity over space and time. It is chaotic and a real challenge to simulate with a computer. In a typical microfluidic device the Reynolds number would be less than 0.1, ($\rho = 1000$ kg/m^3, $v = 0.01$ m/s, $L = 1 \times 10^{-5}$ m and $\rho = 0.001$ kg/m/s). This implies that inertia is quickly damped or absorbed by the viscosity and that there is no turbulence, that is, nothing like the eddy you could observe in a river. Figure 1.1 shows an example of low Reynolds number flow, where there is no time dependence in the flow and no eddies forming behind the posts.

These types of flows exist because of the micro-structured environment. Controlling and observing that flow in a laboratory setting requires a larger, macro-structured environment. We use an inverted microscope and a series of chucks and adaptors to
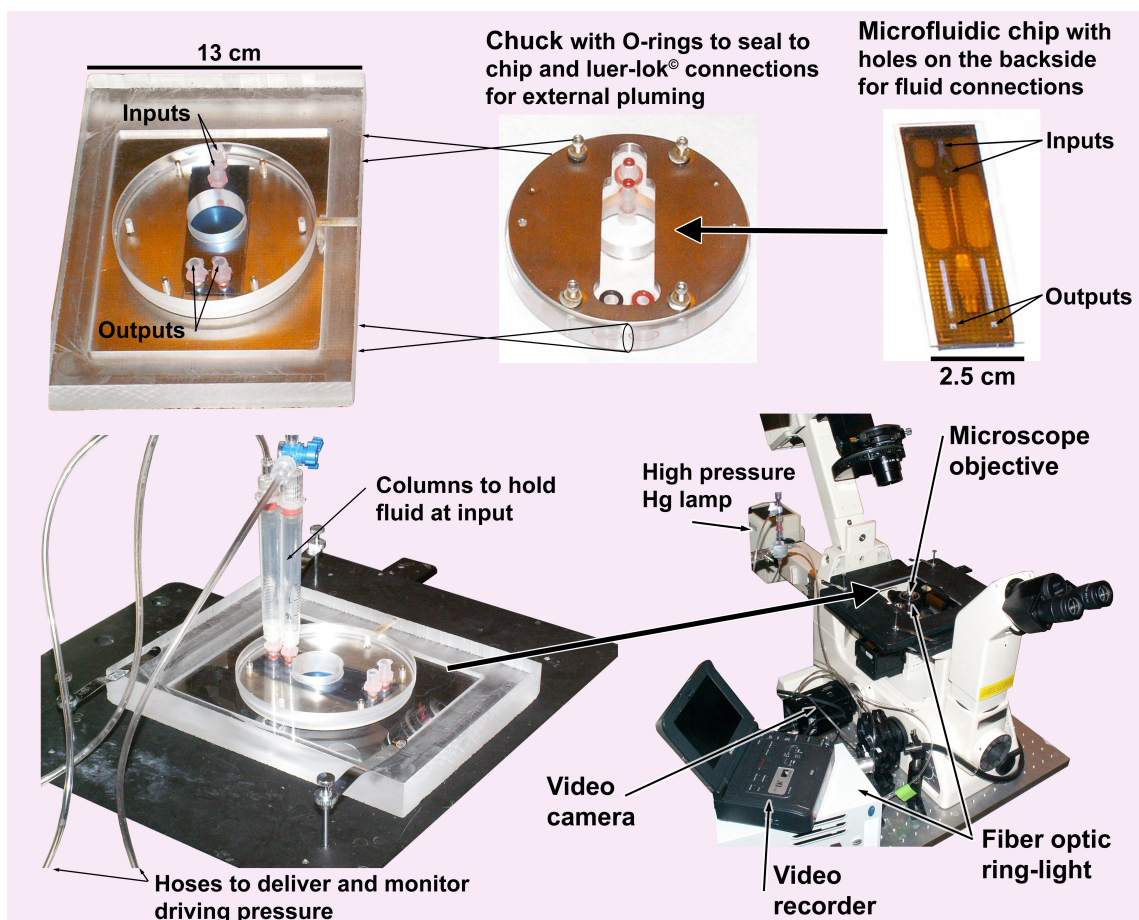
Figure 1.2: Photographs of the laboratory set up for operating and observing the microfluidic device.

observe the flow and separation process during operation, Figure 1.2. The chips are constructed from two pieces: an opaque silicon substrate with holes cut through for off-chip fluid connections, and a glass slide coated with clear silicone rubber. The features that guide the fluid flow are molded into the silicone rubber. We view the on-chip fluid flow through the glass slide and silicone rubber using a long working distance microscope objective. Broad spectrum white light Illumination is provided by a fiber optic ring that sits around the microscope objective. Narrow spectrum illumination for fluorescent imaging is provided by a high pressure mercury lamp.

1.2   Thesis outline

Chapter 2 describes a way of separating magnetically labeled cells from unlabeled cells. The physics of the magnetic force for bead assisted and for separation using the native susceptibility of red blood cells are also summarized. Chapter 3 describes the operating principles of a size-based particle separation method, deterministic lateral displacement (DLD), invented by Lotien Richard Huang et al. in 2004 [5]. Chapter 4 describes the use of that method, to filter particles, such as cells, from whole blood leaving just the plasma. Chapter 5 describes using the DLD method to measure the size of white blood cells. Chapter 6 describes using the DLD method to measure the size of smaller cells in blood (platelets and red blood cells). This combines techniques described in the previous two chapters. Appendix A gives a list of publications and conference presentations arising from this dissertation research. Appendix B give practical details and protocols for carrying out the experimental work described herein.

Chapter 2

Continuous-Flow Cell Separation by Magnetic Forces

2.1 Introduction

Cell separation by centrifugation is performed nearly every time blood is extracted from the body. In a centrifuge, blood is separated along a density gradient. Despite 30 years of research into other means of blood separation, the centrifuge remains the workhorse of hematology laboratories. Microfluidic cell separation and lab-on-a-chip technology may one day change that. This chapter describes two approaches for microfluidic magnetic cell separation and gives details of our work separating blood cells by the selective attachment of magnetic beads to cells.

One key component of the lab-on-a-chip approach is a cell separator. Cell separators can facilitate cell counting and are essential for separating and collecting various cell types. The field of cell separation is not new, and attempts to miniaturize it have begun by modifying existing techniques. The most advanced method for cell separation is flow cytometry.

Flow cytometry is the analysis and separation of single cells by flowing them

past an optical detector that measures fluorescence, and light scatter. A computer makes a decision, based on input from the detectors, whether or not to alter, using an electric field, the trajectory of the falling cell into one of a number of bins. Some notable applications of flow cytometry are: obtaining helper T lymphocyte counts for monitoring HIV treatment, analysis of malignant tumor cells and identification and separation of rare stem cells [6].

Flow cytometry is an emerging diagnostic field, but it is in limited use because the apparatus, involving a number of lasers and detectors, is large and expensive. Magnetic separation is very inexpensive in comparison and can in some cases perform the tasks for which flow cytometry is typically used, such as stem cell, T-cell, and tumor cell isolation [7–9]. While flow cytometry is capable of analyzing and separating based on many markers simultaneously, when one marker is sufficient for separation there is clearly a reason to use a simple, and inexpensive device such as a magnetic separator.

Magnetic cell separation is easily divided into two classes: using magnetic beads to select cell types, and using the native magnetic susceptibility of cells to select cell types. Separation of red blood cells from whole blood by native magnetic susceptibility was first demonstrated in 1975 by D. Melville [10]. Separation by selective attachment of magnetic beads was demonstrated in 1977 by R. Molday [11]. These feats were recently demonstrated on microfluidic devices [12–14]. We discuss the basic principles of how forces are generated via the magnetic susceptibility of an object and how microfluidics can be combined with micron-scale magnetic field gradients to greatly enhance, in principle, the fractionating power of magnetic fields.

The energy of a magnetic dipole $\vec{m}$ in a magnetic field $\vec{H}$ is,

$$U_M = -\mu_o(\vec{m} \bullet \vec{H}). \tag{2.1}$$

From this equation we can derive the force for all cases of magnetic separation.

2.2   Separation by native magnetic susceptibility

While most biological matter is composed of water, a weakly diamagnetic substance, certain cells contain paramagnetic material. The most paramagnetic cell in the body is the deoxygenated red blood cell. In a vacuum the reduced or deoxygenated red blood cell is actually diamagnetic [15,16], but taken against a more diamagnetic background like water or blood plasma, the red blood cell behaves in a uniquely paramagnetic way. This paramagnetic component is formed by unpaired spins in each of the four iron atoms per hemoglobin molecule. This unique property of red blood cells allows for their removal from whole blood using a magnetic field.

The magnetic force on a paramagnetic object such as a red blood cell can be found by replacing $\vec{m}$ in Equation 2.1 with $\chi V \vec{H}$ and taking the negative of the spatial derivative.

$$\vec{F_M} = \mu_o \chi V \vec{\nabla}(\vec{H} \bullet \vec{H}) \tag{2.2}$$

$$\vec{F_M} = 2\mu_o \chi V (H \vec{\nabla} H) \tag{2.3}$$

The susceptibility is χ and the cell volume is V. For a cell in plasma we replace χ with $\Delta\chi = \chi_{cell} - \chi_{plasma}$, the difference in susceptibility between the cell and surrounding medium in Equation 2.3. Takayasu et al. [17] measured the susceptibility of red blood cells, $\chi_{rbc} = 4 \times 10^{-6}$, and blood plasma, $\chi_{plasma} = -8 \times 10^{-6}$ (SI). The susceptibility of water is -8×10^{-6}, which is the same as that of plasma.

High-gradient magnetic separation has been shown to be effective at separating red blood cells from plasma and other cells in whole blood [10,18–20]. Magnetic changes in red blood cells have also been used to separate diseased cells and cells with congenital abnormalities from normal cells [21,22]. These devices typically use

small, ($\sim 24\mu$m diameter) ferromagnetic wire loosely packed into a region near the poles of a large magnet, creating a magnetic filter. When magnetized, the small wires generate high magnetic field gradients that trap the paramagnetic cells. Initially the red blood cells are retained in the high gradient region, while the other cells and plasma are rinsed out. By assuming a reasonable magnetization, or induced magnetic field, for iron of 0.5 T, and having it change direction with the space of 24 microns, we can estimate the field gradient to be in the range of 5×10^4 T/m. When the external magnet is removed or switched off, the red blood cells are flushed out.

Han et al. [12,13] recently showed the continuous separation of red blood cells in a microfluidic device by passing whole blood around a magnetized microfabricated nickel feature. This device, and the accompanying magnet were approximately 10 times smaller than that used by Takayasu et al. in 2000 [20].

2.3 Microfluidic separation via magnetic beads

Immunomagnetic cell separation, which is the use of magnetic beads coated with cell-specific antibodies to separate certain cell types is only about 15 years old, but has blossomed recently as an affordable way of isolating rare cells [8,23–28]. The magnetic beads, ranging in size from 10 nm to 10 μm, are typically a mixture of polymer and iron oxide particles, Fe_2O_3 and Fe_3O_4 and suspended in an aqueous mixture.

When large beads, greater than two micrometers, are used a centimeter-sized rare earth permanent magnet (H $\sim$0.2 T) is capable of holding the labeled cells while the unlabeled cells are washed away. When smaller beads are used, some form of magnetic gradient intensifier, such as the packed ferromagnetic wire described above, is generally required. A number of recent publications have described microfluidic devices for the separation of magnetic beads [29–35], but fewer have successfully sorted or manipulated cells [14,36,37].

2.3.1 The force on a magnetic bead

The linear response, Eq. 2.3, does not generally hold for magnetic beads because their magnetization response is typically non-linear. The magnetization, M, usually increases linearly up to a saturation field, after which no further magnetization is generated with increasing applied magnetic field. This changes the force equation. The saturation field or saturation magnetization is highly dependent on bead size. Beads less than 100 nm in diameter are usually considered superparamagnetic [38]; their lowest energy configuration is to have a single domain per bead in any magnetic field, and are thus always saturated. In liquid it takes a relatively small applied field to align all of the beads to the applied field.

In our experience MACS® microbeads, having an average diameter of around 50 nm, saturate at an applied field of 0.03 T. Figure 2.1 shows the magnetization curve for the magnetic beads used in this experiment. The magnetization was measured at room temperature using a SQUID magnetometer. Larger beads may saturate at higher magnetic fields, and smaller beads at lower applied fields.

For the MACS® microbeads, in an applied fields larger than 0.03 T, we must use a new force equation. We can replace $\vec{m}$ in Equation 2.1 with the saturation magnetic moment, $\vec{m}_s$. The saturation magnetic moment per bead, $\vec{m}_s$, is a vector quantity of constant magnitude, but parallel to $\vec{B}$. This means that the magnetization term can be moved outside of the gradient. Replacing $\vec{m}$ in Equation 2.1 with m_s, evaluating the dot product, and taking the derivative gives the force equation,

$$\vec{F_M} = \mu_o m_s \vec{\nabla} H. \tag{2.4}$$

It is sometimes convenient and may provide some insight to write m_s in terms of a number of Bohr magnetons.

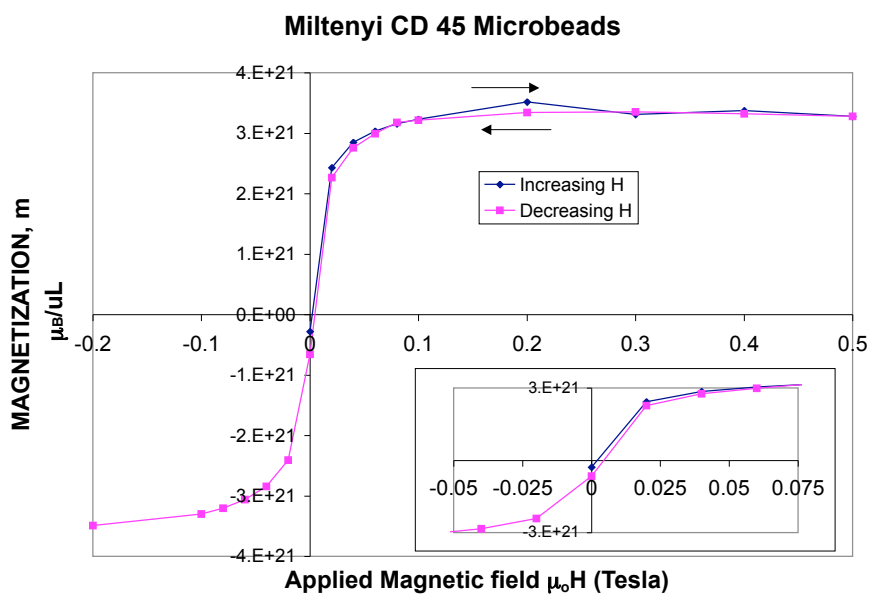$$\vec{F_M} = S\mu_o \mu_B \vec{\nabla} H, \tag{2.5}$$

Figure 2.1: Magnetization curve for Miltenyi MACS® microbeads, as measure by SQUID magnetometry. Saturation occurs near 0.03 T. The manufacturer was unable to supply the number of beads per μL.

where S is the number of bohr magnetons μ_B per bead and H is the magnitude of the applied magnetic field. The force depends on three parameters, the magnetization of the bead, the number of beads per cell, and the gradient of the magnetic field.

Because the magnetization is constant and not proportional to the applied field, the force on the bead is proportional to the gradient of the magnitude of $\vec{B}$. The force is not proportional to the gradient of H^2 or $(2H\vec{\nabla}H)$. This has been misstated or at least confused in the literature more than once [25,28–31,34]. In all cases the authors claim to be using superparamagnetic beads, then give the force equation for a paramagnetic object (Eq. 2.3).

The gradient of the magnetic field is affected by the geometry of the magnetic features. For the stripes used here, increasing their thickness, with constant magnetization, increases the magnetic field. To understand this consider that a permanent magnet can be represented by equivalent charges placed on the pole surfaces. Just like a parallel plate capacitor, as the surfaces move closer together, the field between the plates grows and the field outside the plate shrinks. As the surfaces move apart, the field outside the plates approaches its maximum value. We can generally say that for two otherwise equivalent magnets, the one that is thicker between the poles will produce a larger magnetic field.

2.4   Device operation

We present a continuous-flow microfluidic device that enables cell by cell separation of cells selectively tagged with magnetic nanoparticles. In this design cells flow over an array of microfabricated magnetic stripes, which create a series of high magnetic field gradients that trap the magnetically labeled cells and alter their flow direction. For verification and data collection, the process can be observed in real time using a low power microscope. The device has been demonstrated by the separation of
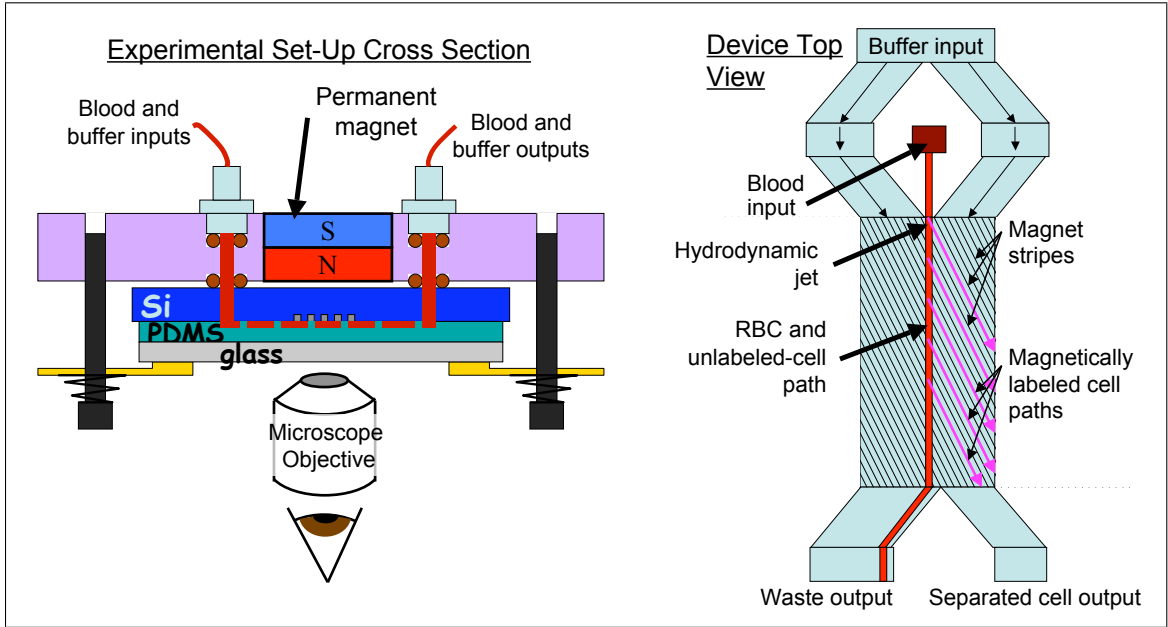
Figure 2.2: Schematic of the experimental set up and a top view diagram of the device showing the cell paths.

leukocytes (white blood cells) from whole human blood. The experimental set up and a schematic of the device showing the paths of separated and un-separated cells is shown in Figure 2.2.

In previous work, cells are either trapped on ferromagnetic fibers which induce locally high magnetic field gradients in a relatively uniform externally applied field and then washed out after the field is removed, or are deflected in a continuous flow by an externally applied gradient of magnetic field in a macroscopic device [7,25,26,29,34].

We present a magnetic cell separator that has two distinct advantages over current methods. First, it is planar and capable of being integrated with other components into a microfluidic total analysis system (μTAS). Further, because it is operating with continuous flow, it can separate a large range of volumes without modification and without periodic flushing of trapped particles or cells. The magnetic field gradients are created by micropatterns of a magnetic material. We also present a numerical analysis of the forces on cells labeled with superparamagnetic beads in such a device, and demonstrate the selective cell by cell separation of leukocytes from blood.

2.4.1 Theoretical analysis

In the device, cells flow over a region of micro-fabricated ferromagnetic stripes (Fig. 2.3(a)) that are recessed into a silicon substrate. The flow is driven by positive air pressure applied to the fluid inputs (Fig. 2.2). The magnetic field pattern from each stripe creates a magnetic trap that alters the movement of only those cells coated with superparamagnetic beads. Cells with a sufficient quantity of beads, i.e. a sufficient magnetic force, become trapped over the magnetic stripes and flow only along the stripe direction, and not parallel to the fluid-flow as all other cells do (Fig. 2.4).

To analyze the forces on the cell we must include the fluidic drag on the cell and sum the contributions of each bead, keeping in mind that each bead on the cell's surface may experience a very different magnetic field. Each magnetic bead is subject to both a force $\vec{F}_{Mz}$ in the vertical direction (z as defined in Fig. 2.3(a)) and a force $\vec{F}_{M\perp}$ which acts in the plane of the device (x as defined in Fig. 2.3(a)). This in plane force, $\vec{F}_{M\perp}$ in Fig. 2.4., will be perpendicular to the stripe. $\vec{F}_{Mz}$ pulls the magnetic bead towards the substrate while $\vec{F}_{M\perp}$ acts to trap the bead in the area above the stripe.

For low Reynolds-number flow, the velocity $\vec{v}$ of a magnetically tagged cell with viscous drag factor η in a flow with bulk flow velocity $\vec{v}_{flow}$ is $\vec{v} = \vec{v}_{flow} + \frac{\vec{F}_M}{\eta}$. This assumes that the fluid flows everywhere with the same velocity. We can identify $\eta\vec{v}_{flow}$ with a drag force $\vec{F}_D$. If the component of the drag force perpendicular to the magnetic stripes $\vec{F}_{D\perp}$ becomes less than the maximum of the magnetic force $\vec{F}_{M\perp}$, (Fig. 2.4) then the cell will be trapped above the stripe because the drag force is not sufficient to push the particle past the stripe. When this happens, the vector component of the drag parallel to the stripe will push the cell along the stripe and it will flow at an angle θ compared to the unlabeled cells. For stripes aligned at an
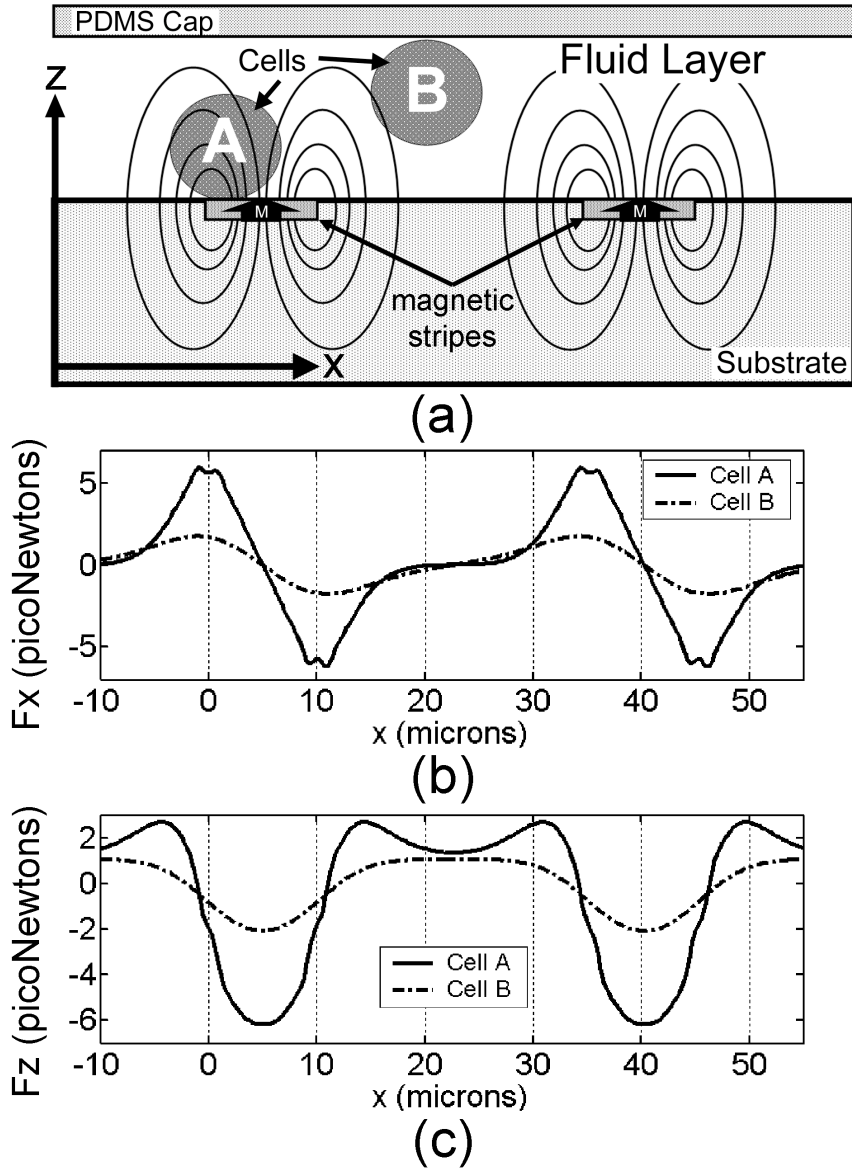
Figure 2.3: (a) Cross section of the magnetic separation device showing qualitative field lines from magnetized nickel structures embedded into a silicon substrate. For simulations, the nickel is 2 μm thick, 10 μm wide at period of 35 μm. (b) Calculated force in the x (lateral) direction on 10-μm diameter cells A (touching surface) and B (center is 10-μm above surface). Nickel magnetization M = 0.08 T, external field of H = 0.08 T, beads of dipole moment m = $1.8 \times 10^5 \mu_B$ and N = 5000 beads per cell was assumed. (c) Calculated force in the z (vertical) direction on cells A and B. The net force per period is negative for both cells.
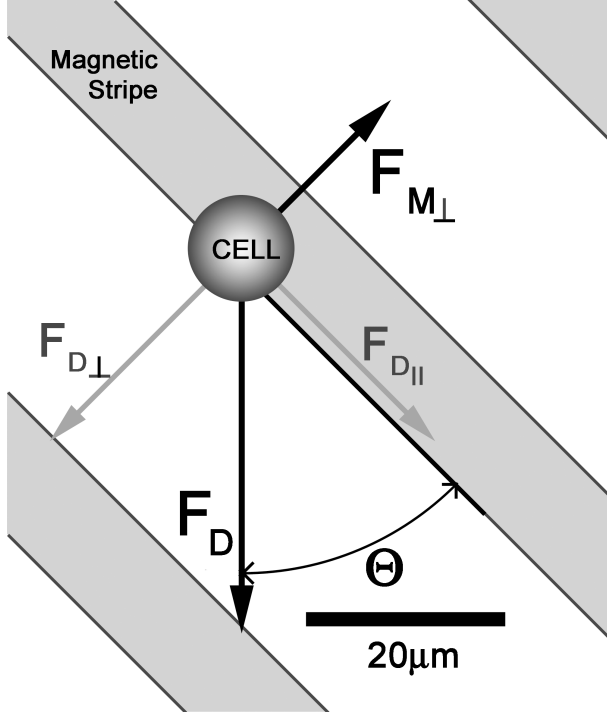
Figure 2.4: Top view diagram of a magnetically labeled cell over a magnetic stripe magnetized out of plane showing in plane magnetic force $F_{M\perp}$ and fluid drag force F_D due to fluid flow at angle θ to stripe direction. F_D is decomposed into components $F_{D\perp}$ and $F_{D\parallel}$ perpendicular and parallel to stripe respectively.

angle θ to the fluid flow the condition for trapping can be expressed as

$$\eta\,\vec{v}_{flow}\sin\theta < \vec{F}_{M\perp max}. \tag{2.6}$$

The magnetic field gradient needed for trapping at a given bulk flow velocity becomes progressively smaller as θ approaches 0°, but the net displacement then also approaches 0. On the other hand, for θ approaching 90° the displacement becomes infinite but the magnetic force $\vec{F}_{M\perp max}$ has to fully balance $\eta\vec{v}_{flow}$ and there is no drag force to push the cell laterally. (Note that even if Equation 2.6 is not fulfilled, cells are slightly deflected as they travel over the stripe, but by an order of magnitude less than if they are trapped [39].) This angle-dependent separation condition provides a possible method for quantifying magnetic properties, such as the number of beads bound to a cell or the amount of paramagnetic hemoglobin contained within a cell.

The magnetic force on a cell in the lateral and vertical directions were modeled assuming 10-μm wide, 2-μm thick nickel stripes at a period of 35 μm with a uniform

out-of-plane magnetization M = 0.08 T, and a uniform external field of 0.08 T. The nickel magnetization was chosen to be set at this level because it was measured experimentally in our structures with an applied field of 0.08 T (in a the same SQUID magnetometer mentioned before). We assumed spherical cells with a diameter of 10 μm, each labeled with 5000 beads (each bead having 1.8×10^5 Bohr magnetons) distributed evenly over the surface. The magnetic moment m was estimated by assuming that each microbead is 50 nm in diameter, 60% by weight iron oxide and 40% by weight dextran [26], and 2.2 μ_B per iron atom. This assumes the beads have a saturated magnetic moment in call cases. Despite the fact that the nickel stripes have a magnetization of 0.08 T, the field generated by them in the fluid is significantly less, and is never strong enough to reduce to net field (applied plus local) to less than the bead's saturation field of around 0.03 T.

Figures 2.3(b) and 2.3(c) show the vertical and horizontal (perpendicular to the stripes) components of the magnetic force on two cells. Cell A is in contact with the magnetic features, while the center of cell B is 10 μm above the wires. The cells are attracted to the center of each magnetic stripe with maximum downward force of 6.2 pN, and maximum force in the x direction of 6.0 pN. For comparison the drag force on a 10-μm sphere held fixed in a 100-μm/s flow using Stokes formula, is 9.5 pN. Thus the trapping and drag forces are comparable. Increasing the magnetic force (by adding more beads or increasing the local field gradient) or decreasing the drag force (by lowering the velocity or lowering the angle) will result in stronger trapping forces.

2.5 Device fabrication

The device consists of a silicon substrate containing recessed magnetic stripes. To fabricate the magnetic stripes, 10-μm wide channels, at a period of 35-μm were etched to various depths into a silicon substrate and then sputter-coated with enough nickel
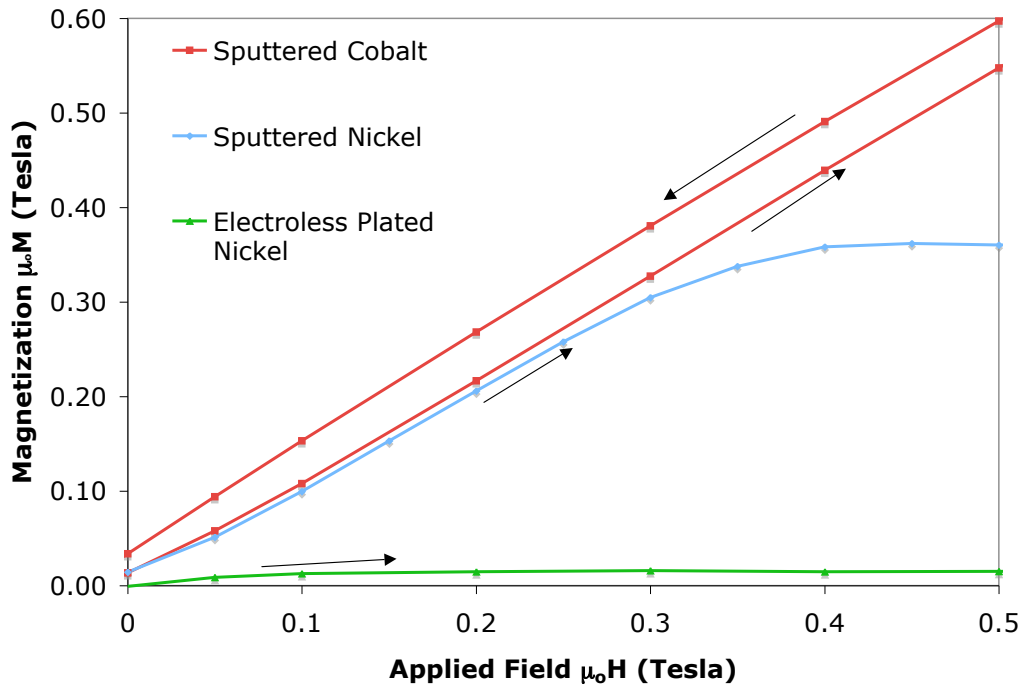
Figure 2.5: Magnetization curves for sputtered cobalt, sputtered nickel and electroless plated nickel features. The measurements were made out of the plane of the wafer.

to fill the channels. The wafer was then chemically mechanically polished (CMP) to achieve a smooth surface with recessed nickel stripes, 2-μm thick, with their surfaces planar with the silicon surface (Fig. 2.3(a)).

We also experimented with electroless plating of nickel (Transene.com, MA USA), in which nickel is deposited onto conducting surfaces from a hot aqueous solution. The elelctroless plating process has the advantages of a higher deposition rate, and a lower cost. Unfortunately the films had poor magnetic properties. Figure 2.5 shows magnetization curves (measure on a SQUID magnetometer) for sputtered cobalt, sputtered nickel and electroless plated nickel features. For the sputtered Co and plated Ni, the features were approximately 5 microns deep and consisted of 10 micron wide stripes at a 35 micron period. For the sputteed Ni, the features were 20 micron squares at a 40 micron period in both directions and also approximately 5 microns deep. The vertical axis is magnetization μ_oM and is independent of size or volume.

19

A 75-nm silicon dioxide layer was then deposited on the wafer surface by plasma-enhanced chemical vapor deposition. A PDMS (polydimethyliloxane) layer containing 15-μm deep microfluidic channels was then sealed to the substrate to direct the fluid flow. A uniform flow of fluid in one direction (at an angle θ to the stripes) was imposed over the substrate by positive pressure combined with a row of microfluidic resistors at the top and bottom of the substrate reference [40]. The cells were injected through a 40-μm-wide aperture in the middle of the microfluidic resistors. An external field H of up to 0.1 T was applied using an NbFeB magnet of dimensions 2.5 cm diameter by 1.9 cm. The magnet was located 1.1 cm behind the silicon substrate. The field was 0.36 T at the poles of the magnet.

2.6   Experiment

To demonstrate operation of the device we labeled cells with CD45 Microbeads from Miltenyi Biotech (Auburn CA, USA). The beads are 20 to 100 nm in diameter and were estimated in the previous calculations to have an average magnetic moment of 1.8×10^5 μ_B. The CD45 antigen is expressed to varying degrees on all leukocytes [41]. Whole, undiluted human blood less than 24 hours old was incubated in a heparin-coated container with a vital nucleic stain, Hoechst 33342 (Hoechst, Frankfurt, Germany) at 100 μg/ml, for 15 minutes at 37 ^{o}C, and then incubated with the Microbeads for 15 minutes at 9°C. After this preparation we expect all leukocytes to fluoresce when illuminated with 300- to 400-nm light, and to be coated with at least 4000 beads [28,42]. To reduce adhesion of the cells to the walls of the device, the device was soaked in a 2 mg/ml solution of Pluronic F108 (BASF, Mount Olive, NJ) and water for at least one hour [43]. During operation, phosphate buffered saline (PBS) containing 2 mM EDTA (ethylenediaminetetraacetic acid) and 2 mg/ml F108 was used.
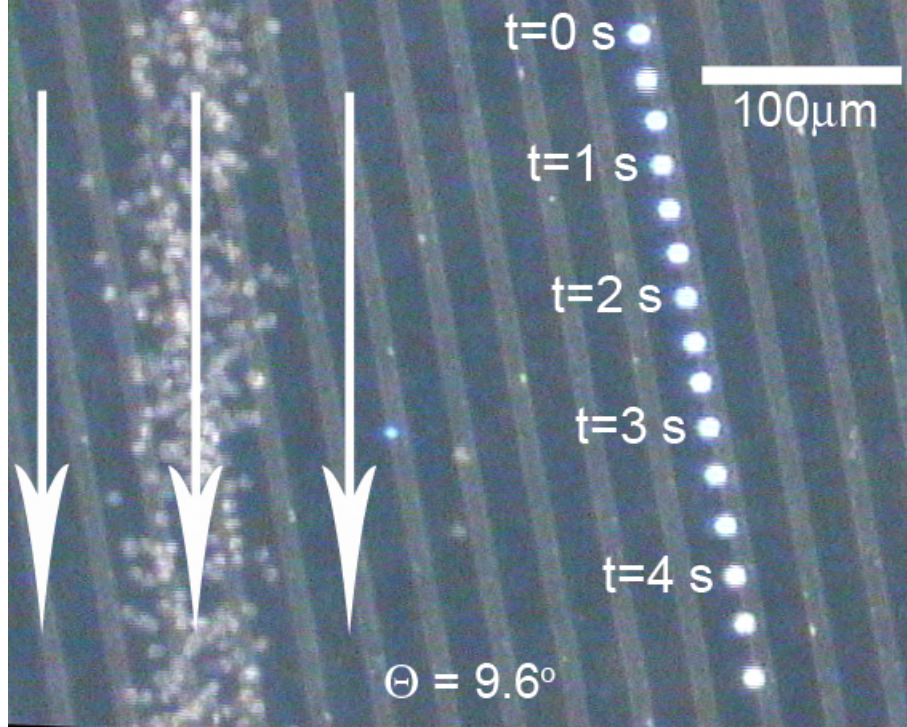
Figure 2.6: Time lapse image showing a single tagged fluorescing leukocyte at different times tracking a magnetic stripe at an angle of 9.6° to the fluid velocity (average of 110 μm/s) indicated by white arrows. Red blood cells on the left are from a single image. All cells entered the chip at the same point approximately 1.5 mm above the field of view.

In Figure 2.6, we present a sequence of images that illustrates the difference in the path of a tagged leukocyte from that of untagged red blood cells. The fluid layer is 15 μm thick, the external field is 0.1 T, and the average flow speed is 110 μm/s, inferred from the red blood cells, which are not deflected. The path of the red blood cells can be seen from the single image which comprises the background of Figure 2.6. Superimposed is the fluorescent image of a single leukocyte at intervals of 0.33 s. The cell has become trapped over the magnetic stripe and follows it, diverging from the untagged cells.

Figure 2.7 shows histograms of multiple leukocyte separations under three different conditions. The lateral positions of the cells are measured with respect to the center of the red blood cell stream (defined as x = 0 μm) after traveling 1.15 mm in the
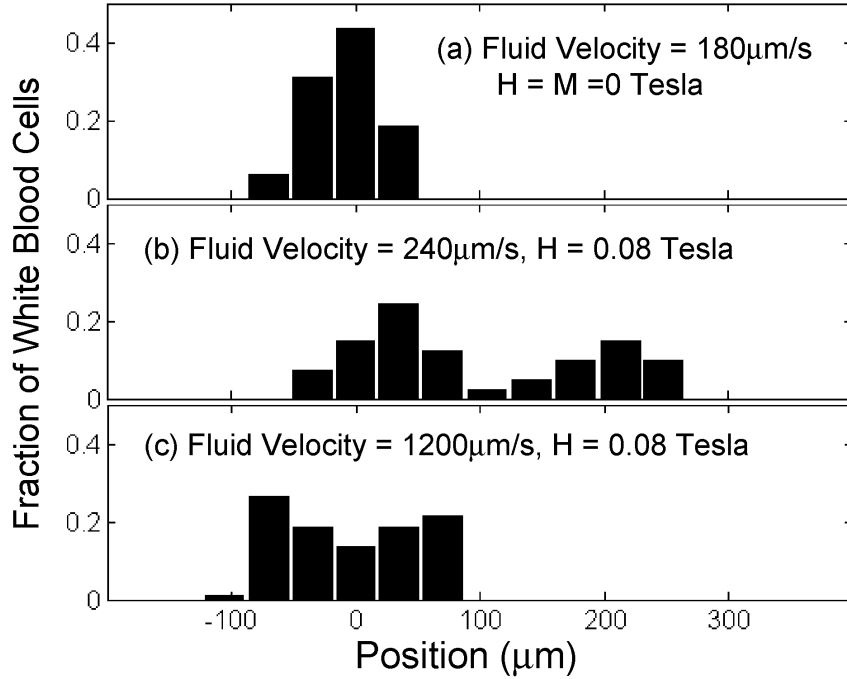
Figure 2.7: Histograms comparing three different operating conditions. The positions of white blood cells are recorded at 1.15 mm into the device with the magnetic stripes at 11° to the fluid flow. The position of the undeflected red blood cell stream is defined as x = 0 μm (a) The external field is 0 T and the fluid velocity is 180 μm/s. The width of the distribution is equal to the width of the red blood cell stream through the device. No separation has occurred. (b) The external field is 0.08 T, and the fluid velocity is 240 μm/s. The peak at 220 μm represents a population of nucleated CD45$^+$ that was separated from the red blood cells by traveling along magnetic stripes. The peak at 0 μm represents nucleated cells that were not separated. (c) The magnetic field is 0.08 T and the fluid velocity is 1200 μm/s. No separation has occurred due to increased drag forces. The width of the peak in (a):$\sim$ 120μm, and (c):$\sim$ 200μm, is approximately equal to the width of the red blood cell stream for each case.

device. The magnetic stripes are tilted at $\theta = 11°$ to the fluid flow and extend up to the beginning of the hydrodynamic jet (1.15 mm upstream). In Figure 2.7(a), the device has been demagnetized, no external magnetic field was applied and the flow speed was 180 μm/s. No separation occurred, and all cells followed the fluid flow direction to exit the camera's field of view at approximately x = 0 μm. The width of the peak is identical to the width of the red blood cell stream.

In Figure 2.7(b) an external magnetic field of 0.08 T was applied, and the flow

speed was 240 μm/s. There is a new peak in the histogram at x = 220 μm, representing 40% of the white blood cells, which corresponds to cells becoming trapped and following magnetic stripes. Cells that exactly follow the magnetic stripes are contained in this peak, centered at 220 μm. Presumably the separation condition given in Equation 2.6 has been met for these cells. We calculate the separation condition to be met when traveling slower than 240 μm/s for $\theta = 11°$ degrees, assuming 5000 beads on a 10-μm-diameter spherical cell on the bottom of the channel. The peak at approximately x = 30 μm contains 60% of all leukocytes; these have been deflected only slightly.

The bimodal distribution seen here, where some cells are separated and others are not, may be caused by variations in the number of beads attached to cells. Table 2.1 shows the distributions of CD45 binding sites on normal white blood cells found by Bikoue et al. in 1996 [41]. Given the data in Fig. 2.7(b) is reasonable that mostly lymphocytes (which would bind more than twice the number of CD45 beads as other cells) were meeting the separation condition and forming the right peak, while neutrophils were not separating because they had an insufficient number of beads attached to them. Other factors which could affect the separation condition include the cell size, larger cells are harder to trap due to increased drag forces, and the possibility of steric exclusion of binding sites, where one bead covers multiple binding sites. Steric exclusion of binding sites may occur on smaller cells, such as lymphocytes, where it would decrease the magnetic trapping force on the cell.

Cell Type	ABC x10^3/cell	% of WBCs [44]
Lymphocytes	217±64	22-50%
Neutrophils	36±16	45-74%
Monocytes	103±44	0.7-7.5%

Table 2.1: Antibody binding capacity of CD45 to the major white blood cell types

In Figure 2.7(c) the external magnetic field is still at 0.08 T, but the flow speed has been increased five fold to 1200 μm/s. In this case no separation has occurred

and again the width of the distribution is equal to that of the red blood cell stream. The failure to separate occurs because the fluidic drag force, which pushes the cells through each magnetic trap, is now five times larger than in Figure 2.7(b) while the magnetic force is unchanged. When this happens, the separation condition, Equation 2.6, no longer holds because of the increased velocity. We believe that with minor modifications such as increasing the thickness of the stripes and increasing the external field, the separation force can be increased by an order of magnitude, allowing for higher throughput and higher recovery.

2.6.1 Railroading cells

Using this technology we are able to control the positions of cells with some precision. While the cells are moving along the magnetic stripes, they are like railroad cars because they stay on the tracks which can travel at a range of small angles to the flow. I have even seen cells form a train by piling up behind one slow moving cell. By merging the stripes in the wafer, cells that are trapped on different stripes can be loaded onto a single stripe and delivered downstream at a precise location. This may be useful for a number of analysis techniques including; a cell detector or counter that uses the magnetic response of the beads to sense the cell [45], single-cell lysis and genomic analysis, and other analyses of cell structure [46].

Figure 2.8 shows a top-view schematic of a magnetic separation device that groups the separated cells onto a single magnetic stripe. The left image shows the hydrodynamic injection of a stream of blood. The center image shows the actual device, which is as wide as a standard glass slide and constructed of glass, PDMS and silicon. The right image shows a stream of blood flowing through the chip and over the magnetic stripes, notice that the magnetic stripes merge onto a single vertical stripe to the right.

Figure 2.9 shows a histogram of lateral displacement of white blood cells separated
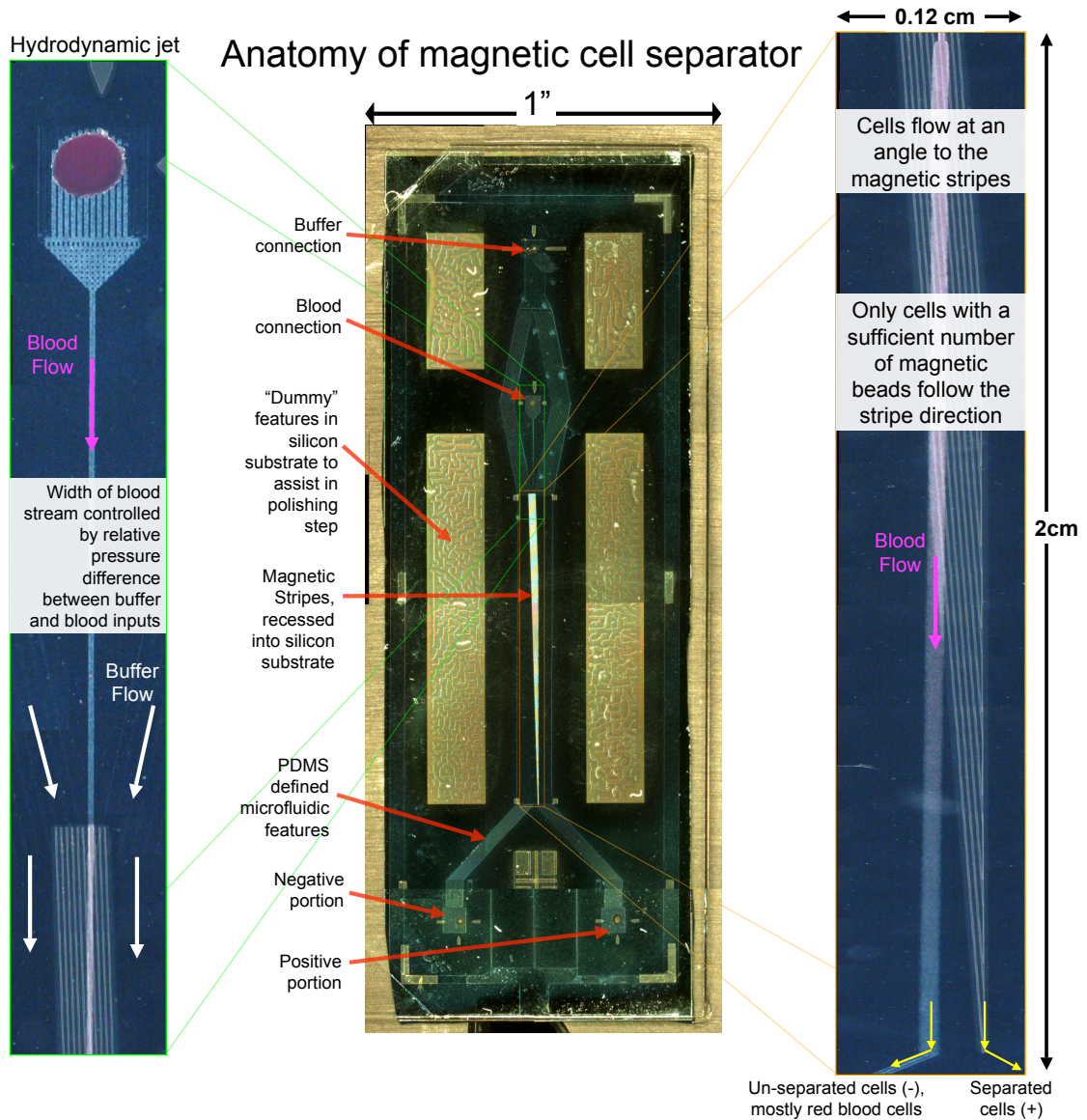
Figure 2.8: A collection of images detailing a version of the magnetic separator. The left image shows the blood entering the device and forming a hydrodynamic jet over the magnetic stripes. The center image shows the entire device. The right image shows the hydrodynamic jet of blood flowing over the entire array of magnetic stripes which merge onto a single stripe to the right.
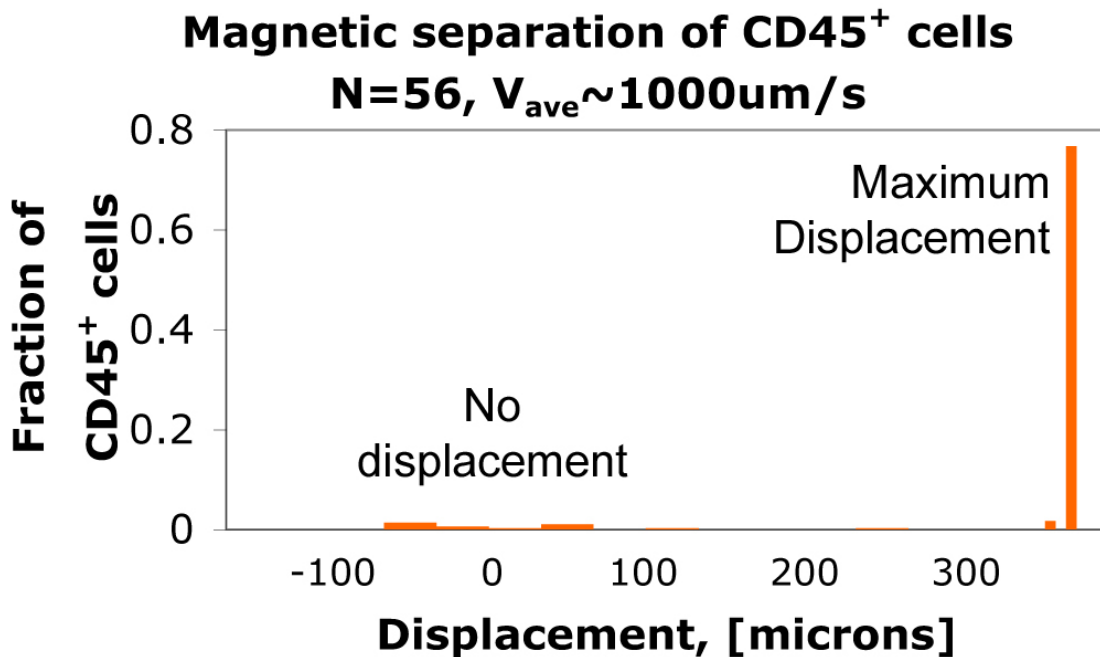
Figure 2.9: Histogram of lateral displacement of white blood cells, (CD45+) labeled with magnetic beads, after passing through the magnetic separator.

in this device. The histogram shows that most of the white blood cells exit the device at the same location. As before, Hoechst 33342 was used to image the cells and CD45 microbeads were used to magnetically label the cells. There is a drastic improvement in the resolution and efficiency of this device over previous devices. Compared to previous devices and previous results, this device has, thicker magnetic stripes (~ 7 versus ~ 2 microns), and a hydrophobic self assembled monolayer (SAM)coating of 11-hydroxyundecylphosphonate (PUL). The PECVD silicon dioxide coating is not necessary when using the SAM layer. This bio-inert and coating was deposited under the guidance of Prof. J. Schwartz in the Dept. of Chemistry. The increase in performance is likely due to less sticking and a stronger magnetic trapping force, resulting in a higher capture efficiency and fewer cells breaking free of the stripes. However, performance decreases with time as cells eventually adhere to the stripes and cause blockages and de-trapping of incoming cells, i.e. train wrecks.

2.7 Discussion of non-ideal behaviour

Numerous non-ideal behaviors were observed. Often cells would pass over multiple stripes before trapping, sometimes being slightly deflected by the stripes, sometimes not. This may result from cells entering the device at some height above the stripes. After a few passes the downward magnetic force has pulled the cells onto the stripe at which point it can begin to follow the stripes.

Cells that were trapped and moving ideally would occasionally release unexpectedly. This may be caused by non-uniform distributions of beads on the cell surfaces (capping) combined with rolling behavior of the cells. Capping is an active process carried out by cells to move labeled surface markers to a single group or cap. Higher fluid velocities in the middle of the channel and zero fluid velocity at the channel wall induce rolling of the object when it is adjacent to the wall. As the cell rolls, there would be moments when the magnetic beads are far from the stripe and thus reduce the magnetic trapping force; the cell could release from the line at this time. Sodium azide, a component in the AutoMACS buffer used, is designed to reduce the capping phenomenom, but we were not able to quantify the distribution of beads on the cell surface. This would be an interesting avenue for future work.

The most significant non-ideal behavior that we observed was the permanent binding of cells to the magnetic stripes. A significant reduction in cell sticking was observed when surfaces were coated with a low energy self assembled monolayer. Even with these coatings, cells readily stuck to any rough or unpolished portions of the magnetic stripes. We used two coatings, both with roughly equivalent results, 11-hydroxyundecylphosphonate (PUL) courtesy of Prof. Jeffery Schwartz in the Dept. of Chemistry, and a fluorosilane, tridecafluoro-1,1,2,2-tetrahydroctyl tricholorosilane. See the Appendix B for a coating protocol for the latter. In my experience, once one cell sticks, others will stick to that one, and still more will adhere to that, resulting a non-functioning device. High fluid speed, more than twice the operating speed, were

sometimes capable of dislodging the stuck cells, but is seemed that the longer they were allowed to remain stuck, the harder they were to remove. Disassembly of the device usually provided strong enough drag and or surface tension forces to dislodge the cells. Clearly more work is needed to create surfaces that cells are unable to adhere to.

2.8   Summary

In summary, we have presented a microfluidic implementation of a device which allows continuous cell by cell separation from a flow stream, by selectively tagging with magnetic beads. The device uses microfabricated magnetic features to induce a lateral force on streaming magnetically tagged cells. The device has been used to separate leukocytes from whole blood and may be useful for integration into some microfluidic total analysis systems.

Chapter 3

Separation by Size: Deterministic Lateral Displacement (DLD) Fundamentals

3.1 Introduction

Cell populations, especially blood, are very complex mixtures, where each cell is a dynamic object, capable of wide ranging behavior. Cell separation by a single parameter, such as the binding of an antibody label has little hope of encompassing this level of complexity. State of the art flow cytometers can quantify the binding of up to 12 different fluorescently coupled antibodies. Separation by size, using the method described in this and later chapters, is simple to operate, potentially inexpensive and high resolution, and is thus another parameter that could help inexpensive microfluidic cell sorters find and identify cells in complex mixtures.

Microfabricated post arrays have recently been used to continuously separate a stream of different sized particles in fluid using a principle known as "deterministic lateral displacement" [5]. In our group these devices have come to be called "bump"

arrays. Previous work has shown that this technique can separate particles of 0.8 to 1.0 micron diameter with resolution as high as one percent. This ability and the simplicity of the device will likely lead to a wide range of applications for both biological and non-biological separations. The goal of this chapter is to provide a theory and experimental measurements of the separation condition where the flow is driven by pressure differential, i.e. hydrodynamically.

Deterministic lateral displacement does not rely on diffusion, but instead, particles above and below a critical size follow different, ideally reversible, predetermined paths through an array of posts (Fig. 3.1). In the array of posts, fluid is driven vertically through rows of posts. The row shift fraction, ϵ is defined as the ratio of the horizontal distance that each subsequent row is shifted, implicitly $\epsilon\lambda$, divided by the array period, λ. For now the vertical row spacing is also λ, so the columns of posts are at a slope ϵ to the average direction of flow. A typical device is shown in Figure 3.2 with a composite image of different bead sizes taking different paths through the device.

3.1.1 Theoretical analysis

As described by Huang et al. (2004), the total fluid flux through each gap can be divided into $n = 1/\epsilon$ flow streams, where n is a whole number. Each flow stream carries equal fluid flux, shown schematically in Figure 3.1. 1 for $n = 3$. The streamlines are separated by stall lines, each stall line beginning and ending on a post. The streamlines shift their positions cyclically so that after n rows each streamline returns to its initial position within the gap. In Figure 3.1 streamline 1 moves to position 3 in the next row, position 2 in the row after that, and finally back to position 1 after three rows. The first and second streamlines are always bifurcated by a post in the subsequent row.

If a particle's radius is larger than the width of the first streamline, the particle will be forced to remain in the second or higher numbered streamline in every row,
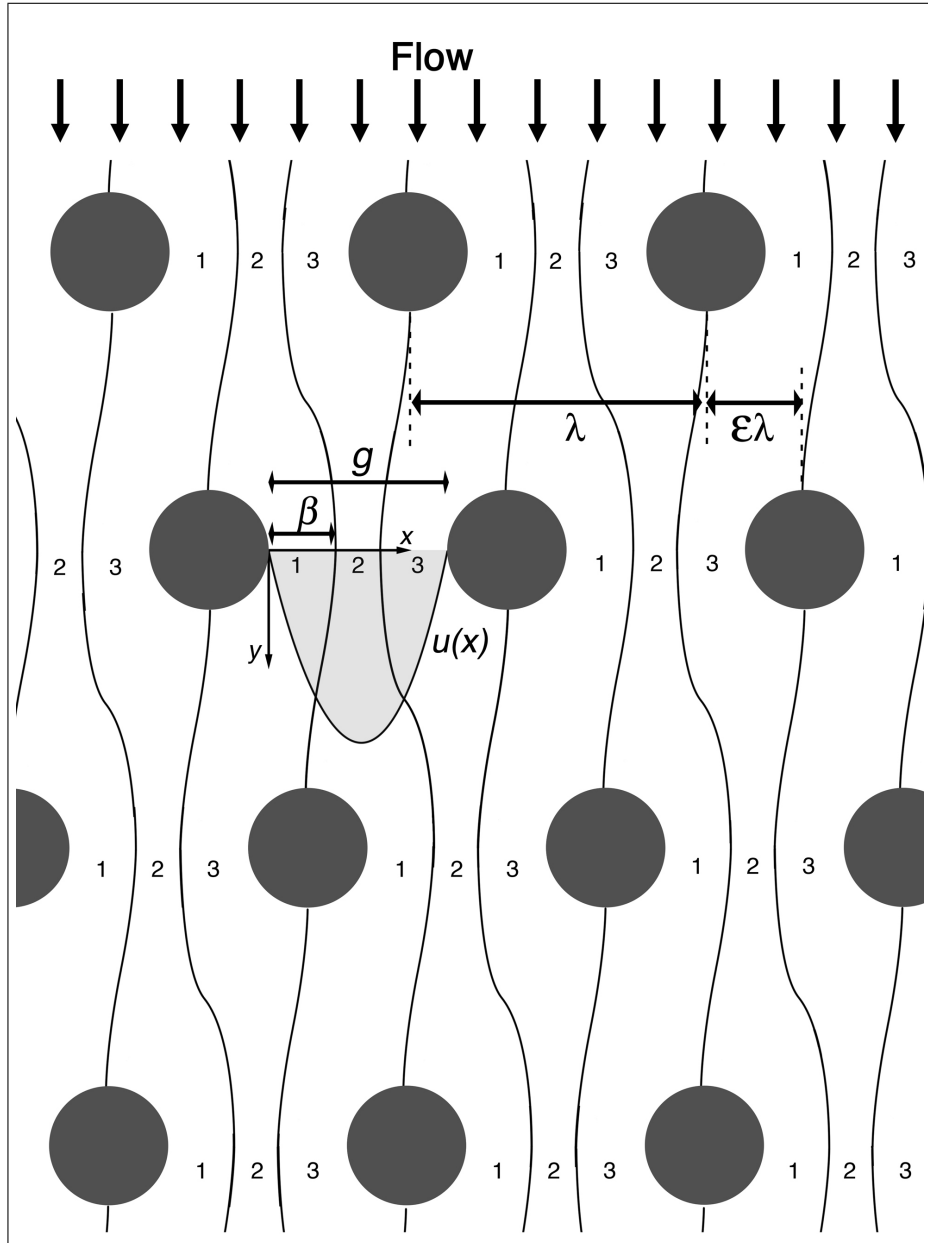
Figure 3.1: Top view diagram of streamlines in low Reynolds number flow through an array of infinitely tall posts. Each row is shifted to the right by one third of the post-to-post spacing, λ, making the row shift fraction, ϵ, = 0.33. Three equivalent streamlines, of equal volume flow rate, flow between each gap, numbered 1 to 3, which cyclically permute from row to row. The streamlines are divided by stall lines which begin and terminate at the posts. An example flow profile $u(x)$ is drawn into one of the gap regions. β is the width of the first streamline.
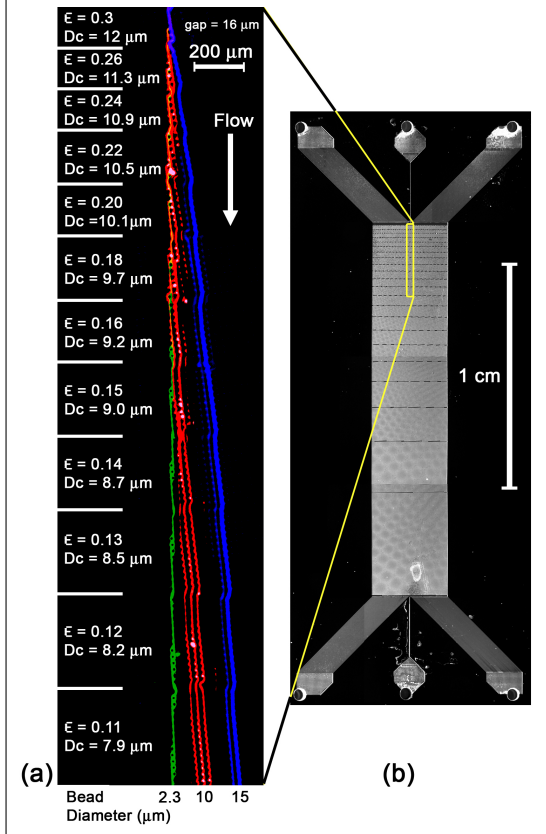
Figure 3.2: False color composite image showing separation of fluorescent polystyrene beads, (a) and photograph of entire device, (b); 2.3-, 10.1-, and 15.0-μm beads are injected in a narrow stream at the top of the array. Each bead population has a a size uniformity of 5%. The critical particle diameter, D_c is decreased in steps by decreasing the epsilon parameter, shown at left. D_c is calculated using the experimental data in Figure 3.4. The 2.3-μm beads (green) are always below the critical size in (a). The 15.0-μm (blue) beads are always above the critical particle size. The size distribution of the 10.1-μm beads is seen in the fourth fifth and sixth regions as the stream of red beads is bifurcated into three streamlines.

as the large particle does in Figure 3.3. (We make the simplistic assumption that a particle follows the streamline in which its center lies.) If it leaves a row in streamline 2, it would normally be carried into streamline 1 in the next row, but since the particle is larger than streamline 1 it is "bumped" into streamline 2. This process repeats at every row, bumping the particle deterministically by $\epsilon\lambda$ at each subsequent row, thus traveling in "bump mode." If a particle's radius is less than the width of the first streamline, it will follow the cyclic procession of the streamlines and travel in "zigzag" mode, as the small particle does in Figure 3.3 and the green beads do in Figure 3.2. This large and small particle move in different directions and are separated.

We now describe how one can analytically determine the critical particle diameter which determines whether a particle bumps or not. The critical particle radius is the dividing line between the two modes of travel and in this model is equal to the width of the first streamline, which we define as β. The parameter of interest is the
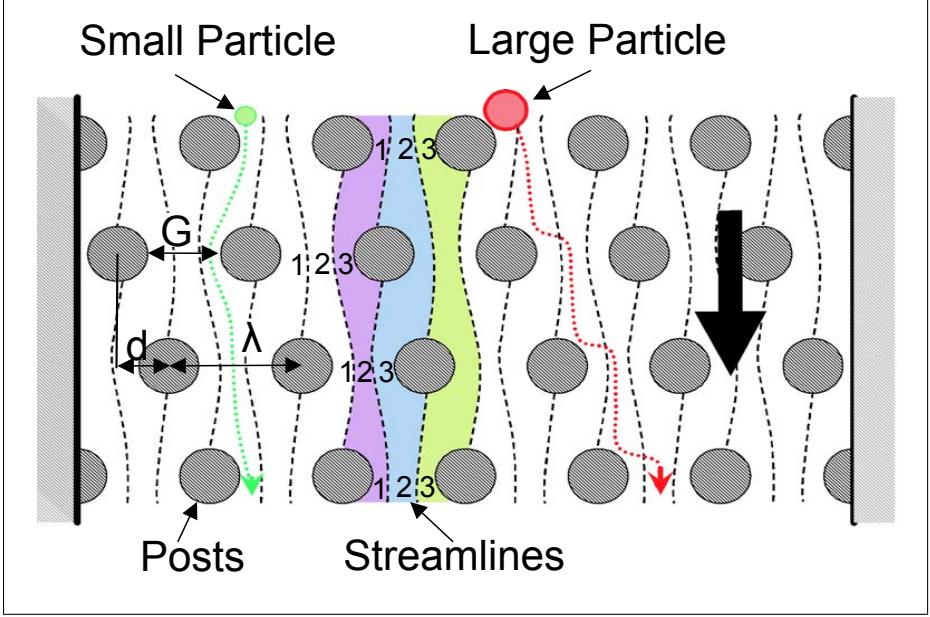
Figure 3.3: Schematic illustrating the two modes of travel for small and large particles through a deterministic lateral displacement device. The dashed lines are the stall lines and form the boundaries between the streamlines. In each gap the streamlines are numbered 1 to n from left to right. *Image courtesy of J. A. Davis [47].*

critical particle diameter, D_c, which is twice the radius or twice the width of the first streamline, β.

The critical particle diameter, D_c, for determining which path a particle will follow is then phenomenologically given by

$$D_c = 2\beta. \tag{3.1}$$

We can replace β to show the effect of the gap, g, and the row shift fraction, ϵ:

$$D_c = 2\eta g \epsilon, \tag{3.2}$$

but then must include the variable parameter η to accommodate for streamlines of unequal widths. If the streamlines are of equal width, each streamline is ϵg wide, but because fluid typically flows faster in the middle of a gap and slower near the

surfaces, the streamlines have different widths.

To calculate the width of the first streamline, and the critical particle radius, for any array we integrate the flow profile, $u(x)$, starting from zero at the post edge to β (Fig. 3.1). Each streamline carries equal fluid flux, but is not necessarily the same width. If β is defined to be the width of the first streamline, then this integral must equal ϵ times the total fluid flux.

$$\int_0^{\beta} u(x)\mathrm{d}x = \epsilon \int_0^{g} u(x)\mathrm{d}x \tag{3.3}$$

The shape of the flow profile determines the widths of the streamlines and thus β. By assuming a conventional parabolic flow profile through the gap, with zero velocity at the post sidewalls, it is possible to analytically find the width of the first stream line, β, as a function of ϵ. Such flow occurs for hydrodynamic flow through a narrow slit [48]. The parabolic flow profile $u(x)$ can be written

$$u(x) = \left[\frac{g^2}{4} - (x - \frac{g}{2})^2 \right]. \tag{3.4}$$

Solving Eq. 3.3 requires finding the cube root of:

$$\left[\frac{\beta}{g} \right]^3 - \frac{3}{2} \left[\frac{\beta}{g} \right]^2 + \epsilon \frac{1}{2} = 0. \tag{3.5}$$

Using $D_c = 2\beta$, one can write the solution to the cubic equation as:

$$D_c = g \left[1 + 2w + \frac{1}{2w} \right], \tag{3.6}$$

where

$$w^3 = \frac{1}{8} - \frac{\epsilon}{4} \pm \sqrt{\frac{\epsilon}{16}(\epsilon - 1)} \tag{3.7}$$

and the correct root of w^3 is

$$w = \left[\frac{1}{8} - \frac{\epsilon}{4} + \sqrt{\frac{\epsilon}{16}(\epsilon - 1)} \right]^{(1/3)} * \left(-\frac{1}{2} - i\frac{\sqrt{3}}{2} \right). \tag{3.8}$$

Two of the roots are real numbers, one is complex, the other real root gives values of D_c that are larger than the gap. An analytical expression for η is then

$$\eta = \frac{D_c}{2g\epsilon}. \tag{3.9}$$

The fraction $\frac{D_c}{g}$ from Equation 3.6 is plotted as a solid line in Figure 3.4 as a function of the row shift fraction ϵ. For $\epsilon = 0.1$ the predicted critical particle diameter is $0.4g$, with $\eta = 2.0$. For $\epsilon = 0.01$ the predicted critical particle diameter is $0.12g$ and $\eta = 5.9$. The surprisingly large critical size at small ϵ is because at small ϵ the first streamline contains only very slowly moving fluid in relation to the streamlines in the middle of the gap so the first streamline must be wider than the others to carry the same fluid flux as streamlines with higher velocities. The parameter η (Eq. 3.9) obtained by assuming a parabolic flow profile (as described by Equation 3.4) is plotted as a solid line in Figure 3.5. The parameter η increases with decreasing row shift fraction, and goes to unity for the largest meaningful row shift fraction, $\epsilon = 0.5$. A row shift fraction of $\epsilon = 0.5$ is not expected to perform any separation. For larger values than 0.5, the array is a mirror image of its former self, with a row shift fraction of $1 - \epsilon$, and where the bump or displacement mode path is at a negative angle to vertical direction.

In the unique case where the flow profile is uniform across the gap (plug flow), each streamline would be $g\epsilon$ wide. Then the critical particle diameter would be $2\epsilon g$, and the η parameter would be unity, shown in Figures 3.4 and 3.5 and as a dashed line. Fluid driven electroosmotically is expected to have a profile more closely resembling plug flow than fluid driven by a hydrodynamic pressure gradient. A combination of

35
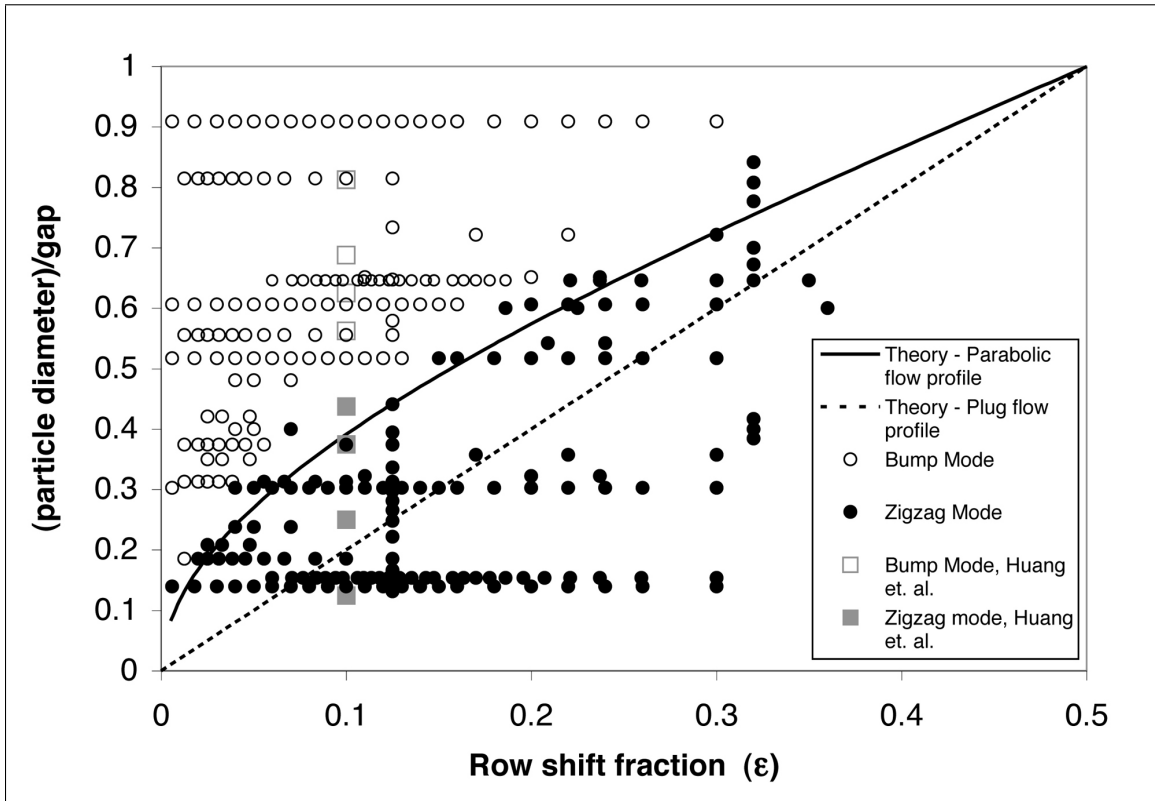
Figure 3.4: Experimental points of the particle diameter divided by the gap, versus the row shift fraction, ϵ. For this work (in black) and that of Huang et. al. [5] (in grey), open points represent bumping mode and solid points represent zigzag mode. Zigzag mode particles follow the streamlines, while bump mode particles follow the array slope, ϵ.
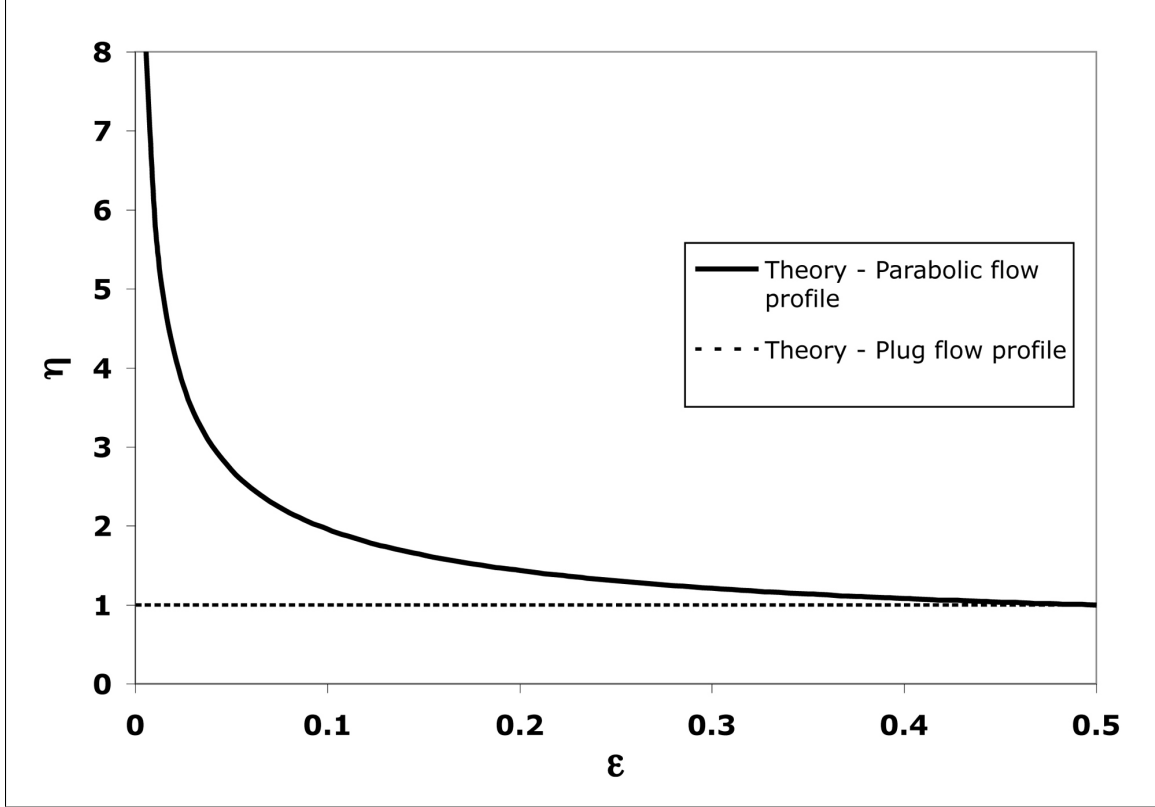
Figure 3.5: Plot of the variable parameter η ($\eta = \frac{D_c}{2\epsilon g}$) which describes the ratio of critical particle diameter to row shift fraction, ϵ, times gap size, g, for both parabolic and plug flow profiles.

electroosmotic flow and pressure driven hydrodynamic flow could result in complex flow profiles with useful critical particle sizes.

3.2 Experiment

Devices with a variety of shift fractions and gap sizes were fabricated so that the effect of changing the shift fraction, ϵ, and the gap, g, on the critical particle size could be observed. The devices consisted of a central region of posts, bounded above by many narrow channels that inject fluid, and below by similar channels to carry fluid away, (Fig. 3.6). Holes were sand-blasted through the silicon substrate to allow for back-side fluid connections.

The lithographically defined values of ϵ ranged from 0.01 to 0.33. The distance

between posts, g, ranged from 12 to 38 μm. The post-size to gap-size ratio ranged from 0.32 to 1.36. The data were collected from polystyrene bead separations of known diameter performed on three separate devices, each with up to 22 combinations of g and ϵ in series. The features of the devices were etched into silicon substrates to a depth of at least 25 μm, with a sidewall angle of less than 2°. The etching was done at the Cornell Nanoscale Science and Technology Facility using a Bosch® process on an inductively coupled plasma etcher.

Achieving vertical fluid flow through the devices is essential, and numerous factors can affect this. Darnton et al. [40] showed that vertical flow and a well-behaved hydrodynamic jet exist in isotropic fluid conductors where the incoming and outgoing fluid fluxes are uniform and identical. More recently, we have found that uniform flux injection does not ensure vertical flow when complex patterns, having anisotropic fluid conduction, exist in the array. We have seen flow moving laterally over multiple post rows at junctions between arrays, and at array-wall interfaces. This does not contradict average vertical flow, which implies the integral of lateral velocity over the entire separation array is 0, just that in some regions it moves one direction and in others it moves back.

The devices were sealed with polydimethyl siloxane (PDMS) coated glass cover slips or glass slides. The devices were soaked in a 2 g/L solution of Pluronic F108. Polystyrene beads with diameters ranging from 2.3 to 22 μm were injected into the arrays through a central reservoir and analyte injection channel (Fig. 3.6). A hydrodynamic jet was formed in the array and the beads were observed to travel in either the bump or the zigzag mode. The average bead velocity was between 500 and 1500 μm/s, achieved by pressure differentials from one end of the chip to the other of approximately 3 to 14 kPa (0.5 to 2 psi). Observations were made using a Nikon inverted epifluorescence microscope (Thunder Bay, CA).

Figure 3.4 shows a collection of points, each one corresponding to one combination
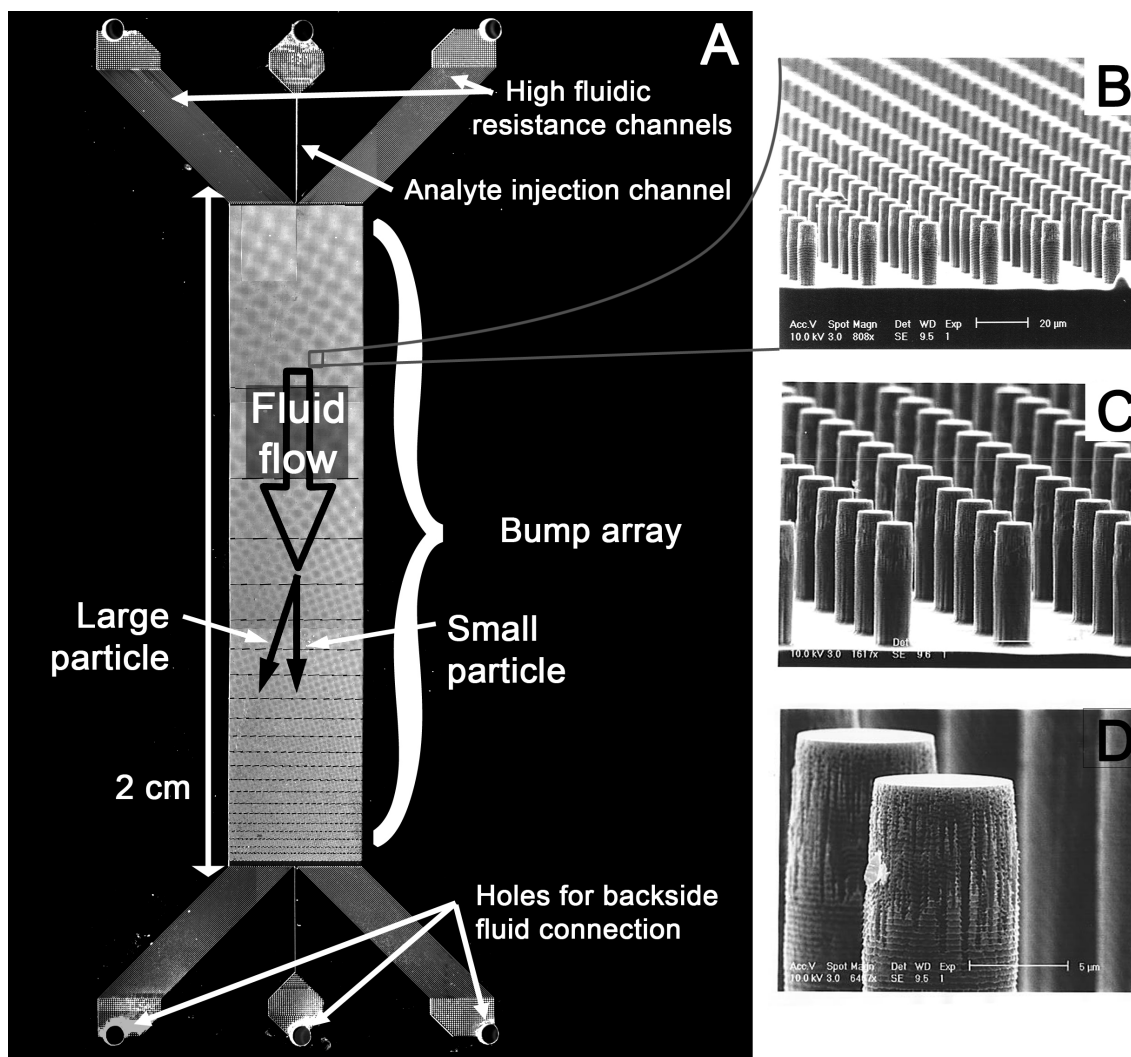
Figure 3.6: (A) Top view image of etched silicon device showing central bump array, high fluidic resistance channels, analyte (bead solution) injection channel, and sandblasted holes for backside fluid connections. Different sections of the array have different row shift fractions and hence appear different in the photo. (B,C,D) Scanning electron micrographs of the posts in the bump array.

of particle size, gap, and shift fraction. The particle diameter divided by the gap is plotted on the vertical axis, and the shift fraction, ϵ, is plotted on the horizontal axis. If the particle moved in the zigzag mode it was plotted as a filled circle. Particles moving in the bump mode were plotted as open circles. Points from Huang et al. [5] are included as grey squares. The distribution in size of the bead populations was apparent on a number of occasions. At 8 of the 297 different combinations of gap, ϵ and nominal bead diameter, the beads showed mixed behavior, some beads traveling in zigzag mode and others in bump mode. These data points are not included in Figure 3.4 for clarity.

There is a clear division between particles which zigzag or bump, with larger particles bumping. As ϵ increases the critical size increases as the width of the first streamline increases.

3.3   Discussion

In Figure 3.4 the general agreement between the theoretical critical diameter (Eq. 3.6) and the experimentally observed dividing line between zigzaging and bumping particles is good. As ϵ increases the critical particle diameter increases. The critical particle size is larger than that implied by plug flow ($\eta = 1$) and in better agreement with that predicted by a parabolic flow profile, as expected for a fluid profile where the fluid velocity is zero at any surface, i.e. a no-slip condition. For fluid flow where the velocity at the post surface is not zero, as in electroosmotic flow, the critical particle diameter is expected to be lower, closer to the plug flow theory. As expected, the results to first order do not depend on flow speed or gap size. Note both models (and the data trend) converge at a critical diameter equal to the gap as ϵ reaches 0.5. In this mostly impractical case there are only two streamlines, each with equal fluid flux, and no separation would occur.

One now has a clear guide for designing the critical particle size in these separation devices. Another important question in bump array design is how to separate a wide range of particles without clogging. What are the limits? In an array of gaps or posts, an obvious limitation is imposed by the size of those gaps. If the device is to work without clogging or jamming, then the gaps must be larger than the largest particles that will enter the array. Now in the same array, having the same gaps, what is the smallest particle that can be "bumped"? We can make ϵ infinitely small, but it is not practical to do so. Small row shift fractions mean a very small separation angle that could be overcome by diffusion and would require very long arrays to achieve separation. We define the range of particles that can be separated as the ratio of the gap size to the size of the smallest particle that is bumped.

In Figure 3.7 we show 5.0-μm particles traveling in the bump mode of an array with a 16.5 μm gap, and $\epsilon = 0.06$. This is a rather small row shift fraction, but serves to demonstrate the concept of separation range. The 2.3-μm particles are below the critical diameter, $D_c = 2.6\mu$m. This demonstrates how an array with a very low ϵ can have a critical particle diameter, D_c, much smaller than the gap. Placing this array in series with arrays of larger ϵ makes the continuous separation of particles over a wide size range possible. We expect, when diffusion and fabrication errors are negligible, that particles with diameters as small as one fifth of the gap should be separable with resolution approaching 1%. This corresponds to a separation range, as define previously, of 5. This improvement in the dynamic separation range may be useful in many areas including the separation of in-homogeneous biological samples. Increasing the separation range of a device comes at some cost though, the length of the device must be increased and size resolution may be lost due to diffusion.
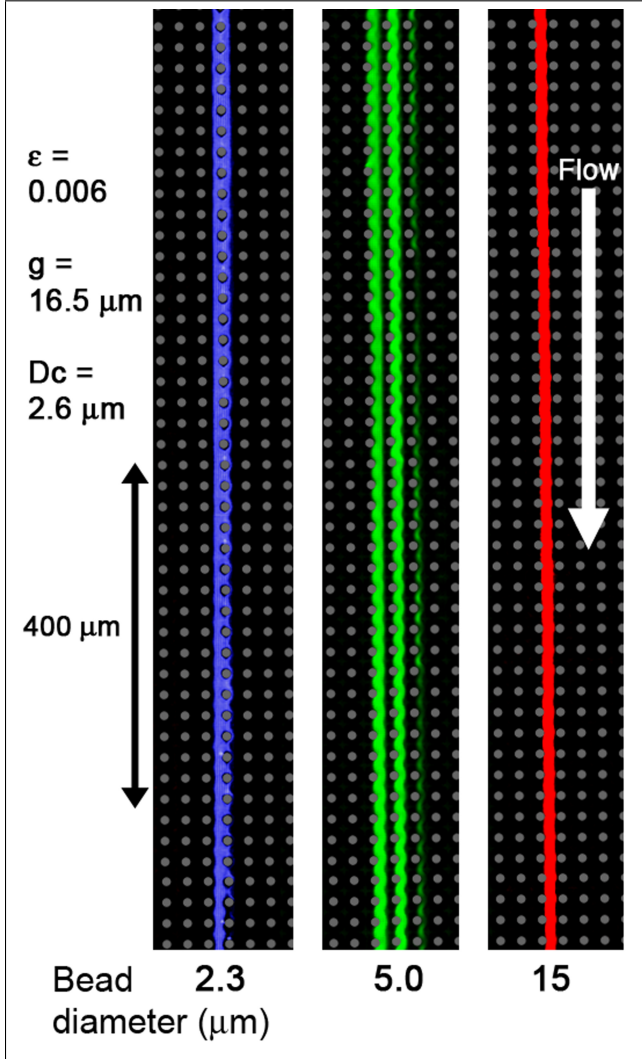
Figure 3.7: False color, time-lapse, images showing zigzag and bump mode flow of fluorescent polystyrene beads in an array with $\epsilon = 0.006$, a gap of 16.5-μm (25-μm pitch), and a critical diameter, D_c, of 2.6 μm. The 2.3-μm beads (blue) are below the critical particle size and thus travel vertically in zigzag mode. The 5.0- (green) and 15- (red) μm beads are above the critical particle size and so travel in bump mode at a slight slope of 0.006 to the vertical flow. Although the 15-μm beads are nearly six times the critical diameter they do not, in general, clog the array and flow through it in zigzag mode. There are more than one hundred 2.3-μm beads shown, between ten and twentry 5.0-μm beads shown, and between five and 10 15-μm beads shown.

3.4 Finite element modeling

The geometry described in Figure 3.1 can be simulated using a graphical finite element analysis package such as COMSOL Multiphysics (MA, USA). The finite element method breaks a complex geometry into many smaller, often triangular, discrete regions and approximates the difficult to solve partial differential equation with a simpler equation having a numerically stable solution in each discrete region. The package solves, among others, the steady state Navier-Stokes equation for incompressible
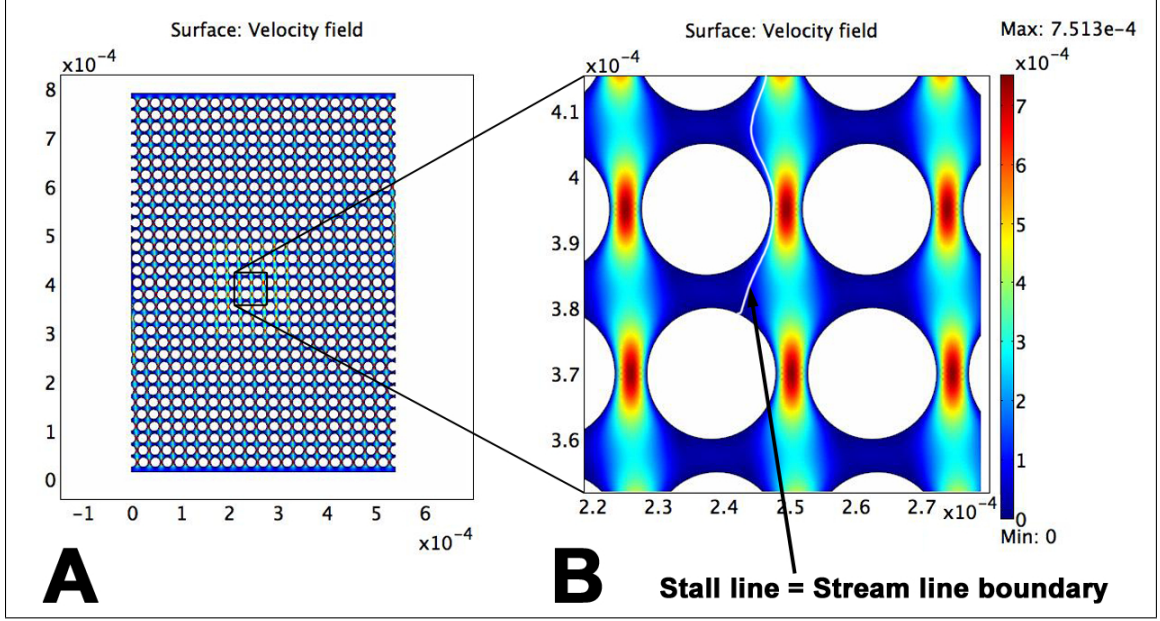
Figure 3.8: Example of a "bump" array model. The model is 22 posts wide and 31 posts long, the posts are 20 microns wide with a 5 micron gap, and arranged with a slope of 1/30 to the vertical walls. The central region of (A) is more finely discretized than the surroundings to conserve memory (B) is a blow up of the central region showing the stall line used to determine the critical particle size.

fluid.

$$\rho \underbrace{(\vec{v} \cdot \triangledown \vec{v})}_{\text{Convective acceleration}} = \underbrace{-\triangledown P}_{\text{Pressure gradient}} + \underbrace{\mu \triangledown^2 \vec{v}}_{\text{Viscosity}} + \underbrace{f}_{\text{Other forces}} \qquad (3.10)$$

This equation has the same form as Newton's equation of motion, with mass times acceleration on the left and forces on the right. Here ρ is fluid density, $\vec{v}$ is velocity, P is pressure, and μ is viscosity.

Models are created by specifying the fluid velocity at the top and bottom boundaries, usually $v_x = 0$ and $v_y = -100 \ \mu m/s$, and making all other surfaces "no-slip", i.e. $v_x = v_y = 0$. Figure 3.8 shows an example model of a bump array with slope $(\epsilon) of 0.033$. The stall line shown in (B) represents the boundary between the 1st and 2nd streamlines in the first row of posts shown in B. It is 0.595 μm from the left post edge. The distance from the left post edge is 1/2 the critical particle diameter. The distance shown in the model corresponds to $D_c/g = 0.24$, which is slightly larger than that predicted by parabolic flow (Fig. 3.4). Unfortunately, in this model, like

all models simulated, the stall line position changes with location in the array. For example, in this same model $D_c/g = 0.19$ ten rows above the position shown, a 20% difference. This change correlates with the presence of lateral flow at the post-wall interface. When posts are touching, but not separated from the wall, fluid is forced laterally away from the wall, increasing the width of the first stream line. This effect may lessen further from the wall.

Ensuring vertical average flow, not just over the entire array, but also within each unit cell, is obviously important. Without it the critical particle size may vary and the resolution of any separation array is reduced. Huang et al.'s 2004 paper [5] used post arrays that were created by rotating a square lattice of posts, the unit cell still being a square. The majority of arrays designed, modeled, and tested since then have been rhombic arrays, where the rows are horizontal and perpendicular to the flow. This geometry is depicted in Figure 3.1. The change was made to facilitate the stacking of many arrays with slightly different row shift fractions.

Furthermore, there is a difference between the two array designs in the way they conduct fluid. In a square array of circular posts where rows and columns are orthogonal and equally spaced, the conductivity of fluid in the row direction or column direction is equal (defined as σ_o). The conductivity at any angle θ to the rows or columns is $\sigma_o(\sin(\theta) + \cos(\theta)) = \sigma_o$, where σ_o is the conductivity in the row or column direction. This is an isotropic conductor of fluid.

For a rhombic array like that shown in Figure 3.1, the horizontal conductivity would still be approximately σ_o, but the vertical conductivity would be slightly less than before. This is because a small amount of fluid, the flux of streamline 1, must pass though an additional constriction. Here we have conductivity in orthogonal directions that is not equal, i.e. an isotropic conductor. Intuitively the easiest axes of conduction in Figure 3.1 would be the horizontal and that which follows the columns of posts. Similarly, cubic crystals are isotropic conductors of light and electrons, where

as hexagonal, tetragonal, and rhombohedral crystals are anisotropic conductors of light and electrons [49].

Ensuring vertical flow is more difficult when using an array that is an anisotropic conductor of fluid. The approach described by Darnton et al. [40] is essential here. To prevent fluid from preferentially flowing along the column direction we must supply equal current injection along the top and bottom of the array without spaces or any low resistance regions between the array and the injectors where the injection velocities can re-arrange. When the separation array has small gaps with very high fluidic resistance, it may be impractical to fluid injection and fluid drainage tubes with even higher resistance since these would have to be much, much longer than the actual separation array.

3.4.1   The post-size to gap-size ratio

The post size to gap ratio also affects the critical particle size. For very small posts relative to the gap, the flow profile broadens, lowering the critical particle size. For very large posts relative to the gap, the profile approaches a parabola, the well know result for a cylindrical tube. Figure 3.9 shows the normalized flow profile in the gap for two simulated structures, having post-to-gap ratios of 0.1 and 10. The critical particle size for these two flow profiles is 0.31 and 0.38 of the gap respectively, $\epsilon = 0.1$ for both. The analytic model described earlier predicts a critical particle size to gap ratio of 0.38 for $\epsilon = 0.1$. Using a small post to gap ratio decreases the critical particle size, while also reducing the fluidic resistance; however it is not usually practical since it requires more challenging lithography and may limit the depth of the device.

3.4.2   Skew

We have experimented briefly with one other variation on the typical bump array geometry. A skewed array is a rhombic array with reduced row spacing, H, and
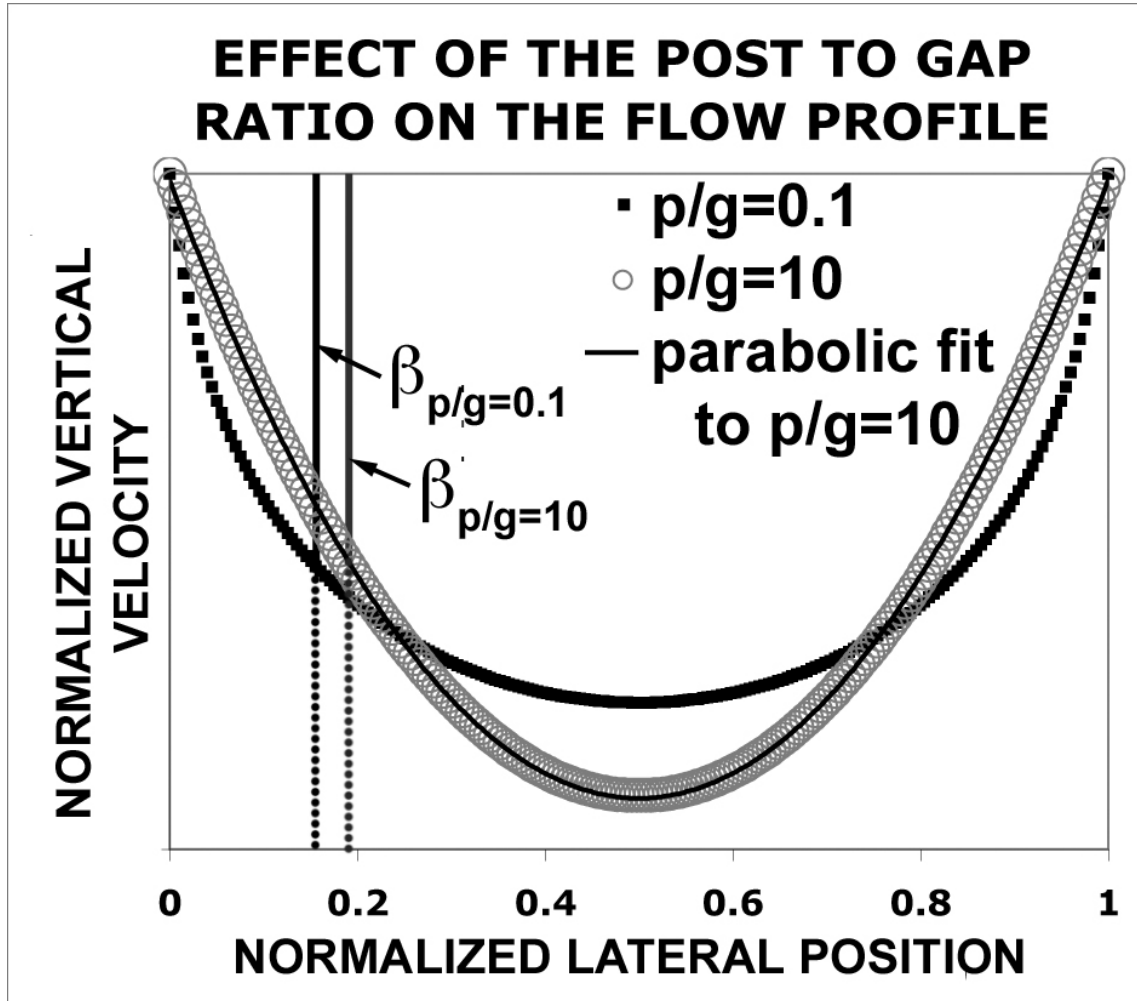
Figure 3.9: The flow profile through the gap for two simulated structures, one having a 1-μm post and a 10-μm gap, ($p/g = 0.1$), the other having a 10-μm post and a 1-μm gap, ($p/g = 10$). For large posts relative to the gap, the profile approaches a parabola, grey circles. The β points for each profile, solid vertical black lines, designate the edge of the first streamline in an array with $\epsilon = 0.1$. They correspond to a critical particle size, D_c, of 0.31 (2×0.156) for the small post model and 0.38 (2×0.191) for the large post model.

increased column spacing, λ. This results in a parallelogram-shaped unit cell. Now the shift from row to row is $H \tan(\theta)$, where θ is the angle that the columns make to the average fluid flow. The critical particle size can still be written

$$D_c = 2\epsilon' g\eta \tag{3.11}$$

where

$$\epsilon' = \frac{H \tan(\theta)}{\lambda} \tag{3.12}$$

and η can be looked up from Figure 3.5 using ϵ'. This approach makes the anisotropic conductivity problem described earlier more significant and results in a negligible reduction in D_c because of the rapidly increasing η parameter with very small ϵ.

3.5   Summary

The fractionation of small particles in a liquid based on their size in a micropost array by deterministic lateral displacement was recently demonstrated with unprecedented resolution [5]. In this chapter we have presented a model of how the critical particle size for fractionation depends on the micropost geometry, depending specifically on the gap between posts, the offset of posts in one row with respect to another, and whether the fluid is driven by hydrodynamics or by electroosmosis. In general the critical particle diameter is much smaller than the gap, which prevents clogging. The model is supported by data with particles from 2.3 to 22 μm.

Devices with a parabolic flow profile through the gap due to pressure driven flow have a larger critical diameter than that expected for fluid driven by electroosmotic flow. A wide range of experiments under pressure driven conditions support the parabolic flow model. Numerical modeling of the flow patterns also supports the parabolic flow model, but experimentally determined critical particle sizes are still

larger than that predicted by the model. We have also briefly considered the effect of the post to gap size ratio and the effects of square, rhombic, and parallelogram array geometries. We have not considered deformation of the flow profile caused by the particle itself. These experiments indicate a maximum possible separation range (ratio of largest to smallest particles that can be differentially bumped) of around 5 in a single array. Separations with a larger range can be accomplished by using multiple devices, which is described in Chapter 4.

Chapter 4

A Continuously Operable Blood Filter: DLD with Extended Range

4.1   Introduction

Cell separation is performed in a centrifuge to some component of nearly all blood that is taken from a patient or donor. A centrifuge separates blood components according to their relative density by subjecting the blood to centripetal acceleration that is a few hundred times stronger than gravity. Blood products such as red blood cells (erythrocytes), white blood cells (leukocytes), platelets, (Fig. 4.1), and plasma are regularly separated in this way and used for treatment and diagnosis of illness.

Automated and somewhat portable methods for preparing blood products from donors are now available. Apheresis allow donors to give only the needed blood component, returning the remaining blood components to the donor. This allows for larger amounts of the product to be collected with less impact on the donor. Apheresis uses a continuous-flow centrifuge to collect red blood cells, for example, while returning most of the plasma and white blood cells to the donor. Figure 4.2 shows schematics for apheretic donation of red blood cells and platelets. Blood products
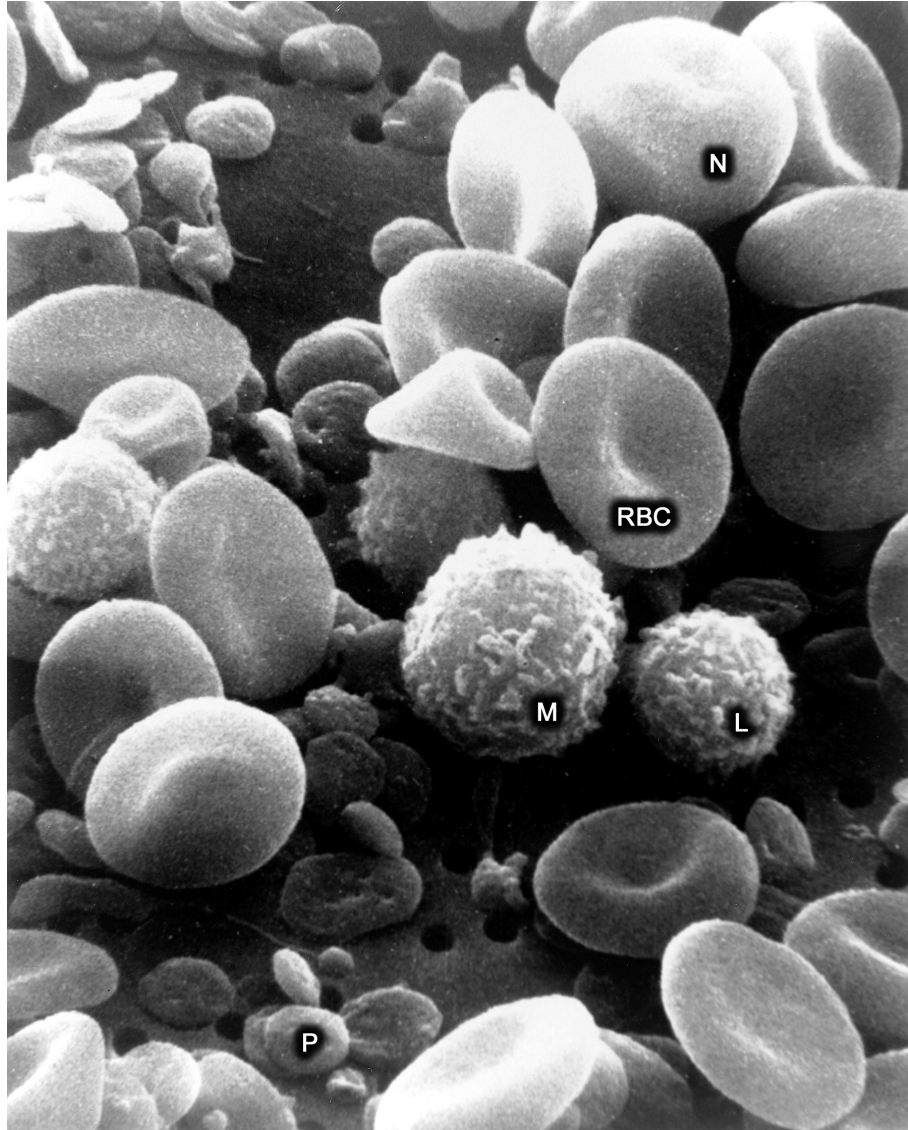
Figure 4.1: "This is a scanning electron microscope image from normal circulating human blood. One can see red blood cells [RBC], several white blood cells including lymphocytes [L], a monocyte [M], a neutrophil [N], and many small disc-shaped platelets [P]." National Cancer Institute (http://visualsonline.cancer.gov/details.cfm?imageid=2129, viewed 5/31/2007) Photographer: B. Wetzel and H. Schaefer.

A) Red Blood Cell Donation

Blood Draw

Donated Red Blood Cells

Return to Donor

Whole Blood

Platelets, WBCs and plasma

P

PRP
WBC

RBC

+

Saline
To replace lost volume

Centrifuge

Image of centrifuge from: http://library.med.utah.edu/WebPath/ TUTORIAL/BLDBANK/BBAPHER.html accessed April 2007

B) Platelet Donation

Blood Draw

Return to Donor

RBCs

Whole Blood

Platelet rich plasma

+

Plasma

Remove WBCs

Remove WBCs from platelets by: Filtering, elutriation, or periodic adjustment of siphon position in previous steps.

P

PRP
WBC

RBC

Plasma

Platelets

Centrifuge

Donated Platelets

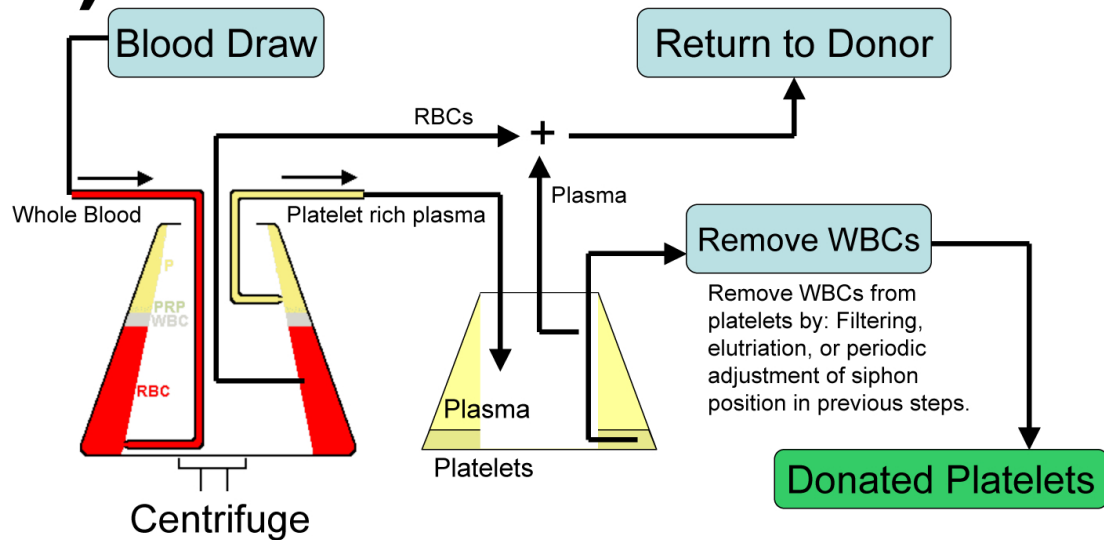Figure 4.2: Flow charts for the apheretic donation of red blood cells (A) and platelets (B).

can also be prepared from of whole blood after donation.

Separation and sorting of blood cells and components is vital for medical research, treatment and diagnostics. The centrifuge, which separates objects by density, has served these needs well, but new methods that do not rely on density differences are being used. Filters made of cotton batting are used to remove white blood cells from donated platelets [50], and flow cytometry and magnetic cell separation are used to separate rare and hard to identify cells [51].

The method for size-based particle separation described in the previous chapter naturally lends itself to blood separation. A paper, co-written by J. A. Davis, myself and others [47] described two approaches: one that measures the size of cells for diagnostic purposes, by processing a narrow stream of blood, and another, designed for higher throughput, that filters the cells from a wide stream of blood to produce plasma. The later device is described here.

4.2   Blood cells as particles

Blood is composed of cells (isolated micron-sized bodies) and plasma. The distribution of cells is given in Table 4.1. Plasma, a yellowish liquid containing essential nutrients and other proteins, constitutes a little over half the volume of blood. The rest of the volume is made up of cells, at least 90% of which are red blood cells.

One of the most common and simplest separations performed on blood is the removal of cells, leaving the plasma or serum.[i] Centrifuging at 1000g (1000 x the acceleration of gravity at Earth's surface) for 5 minutes will cause all of the cells in blood to settle, leaving a liquid supernatant.[ii] Red blood cells and one type of white blood cell settle first, then other white blood cells, and finally platelets. Plasma and serum are used in a wide range of tests and it would be convenient in some

---

[i]Serum is the liquid portion of blood that remains after clotting; plasma is the liquid portion of anticoagulated blood.

[ii]Supernatant means floating above and is an adjective for any liquid above solids or precipitates

Cell Type	Cell Shape	Diameter (μm)	Concentration (μL^{-1})
Platelet	various, discoid to spheroid	$1 - 5$	$50 - 100 \times 10^3$
Red Blood Cell	biconcave discoid	2×7.5	$4.0 - 5.5 \times 10^6$
White Blood Cell	spheroid	$5 - 15*$	$4 - 10 \times 10^3$

Table 4.1: The major components of blood. A more detailed description of platelet and red blood cell morphology is given in Chapter 6. *A small fraction (<5%) of circulating white blood cells are larger than 15 microns in diameter, generally becoming rarer with increasing size.

circumstances to produce them without a centrifuge–for example, in an integrated miniaturized blood diagnostic device.

In this chapter I describe a microfabricated device that separates cells from plasma. Two other microfluidic plasma separation devices have been demonstrated. VanDelinder and Groisman [52] used cross flow filtration, similar to tangential flow filtration (both are conventional methods for large volume filtration). The device produced 1 microliter of plasma per minute, though only separated 10% of all the plasma. Yang et al. [53] used the Zweifach-Fung (ZF) effect, which is very similar to the pinched flow (PFF) and branched flow (BFF) fractionations demonstrated by Yamada and Seki [54–56]. These effects (ZF, PFF, BFF) are similar to DLD because they use stall lines to exclude large particles from certain paths. Their device collected up to 35% of the plasma, but only by first diluting the blood 5 times. The flow rate was as high as 4 microliters per minute at the input. Centrifugation removes 98–99% of the plasma without contamination or dilution and can process large volumes rapidly, so any new will have to fit some particular microfluidics need. We have demonstrated a device that requires no dilution and introduces only diffusion-limited contamination of the plasma.

4.3 Device design

The range of sizes that can practically be separated in a DLD array is not more than 5, i.e. the smallest particle to be separated cannot be smaller than one fifth of the gap. This poses a problem for using the technology with blood because blood has particles that differ in size by more than a factor of 5. If we started with an array having a 20 micron gap, the smallest particle that would be separated would be 4 microns, i.e. 1/5 of the gap. A second array is needed to separate the platelets and, depending on how they behave, the red blood cells. The second array would have a gap of around 5 microns, but most of the cells separated in the previous array would clog this array if allowed to, so they must be carried away, diverted, in an alternate non-clogging path. Figure 4.3 shows a schematic of this idea. Here three separation arrays each with decreasing critical particle size and feature size are cascaded.

Correctly designing this non-clogging path requires understanding and controlling the fluidic resistance of the structures and the pressure drops that occurs in them. For electrical conduction resistance is defined as the drop in voltage over the current, or rate of charge flow. Resistance for fluid conduction is similarly defined as the drop in pressure over the flow rate. Since all of our structures are planar, it is convenient to think in terms of the resistance per unit width in the device, where we are averaging over some distance that is larger than the feature sizes.

All other things being equal, with pressure P_3 at the inputs and pressure P_0 at the outputs ($P_3 > P_0$), if the alternate non-clogging paths have channels with gaps that are significantly larger than the gaps in the separation areas that they bypass, then the resistance per unit width in the alternate path will be much less than in the separation area, the velocity in the alternate path will be much higher than in the separation area and most of the fluid will be siphoned into the non-clogging paths. This will cause non-vertical flow in the separation regions and degrade the device's performance by changing the critical particle sizes in the regions of non-vertical flow.
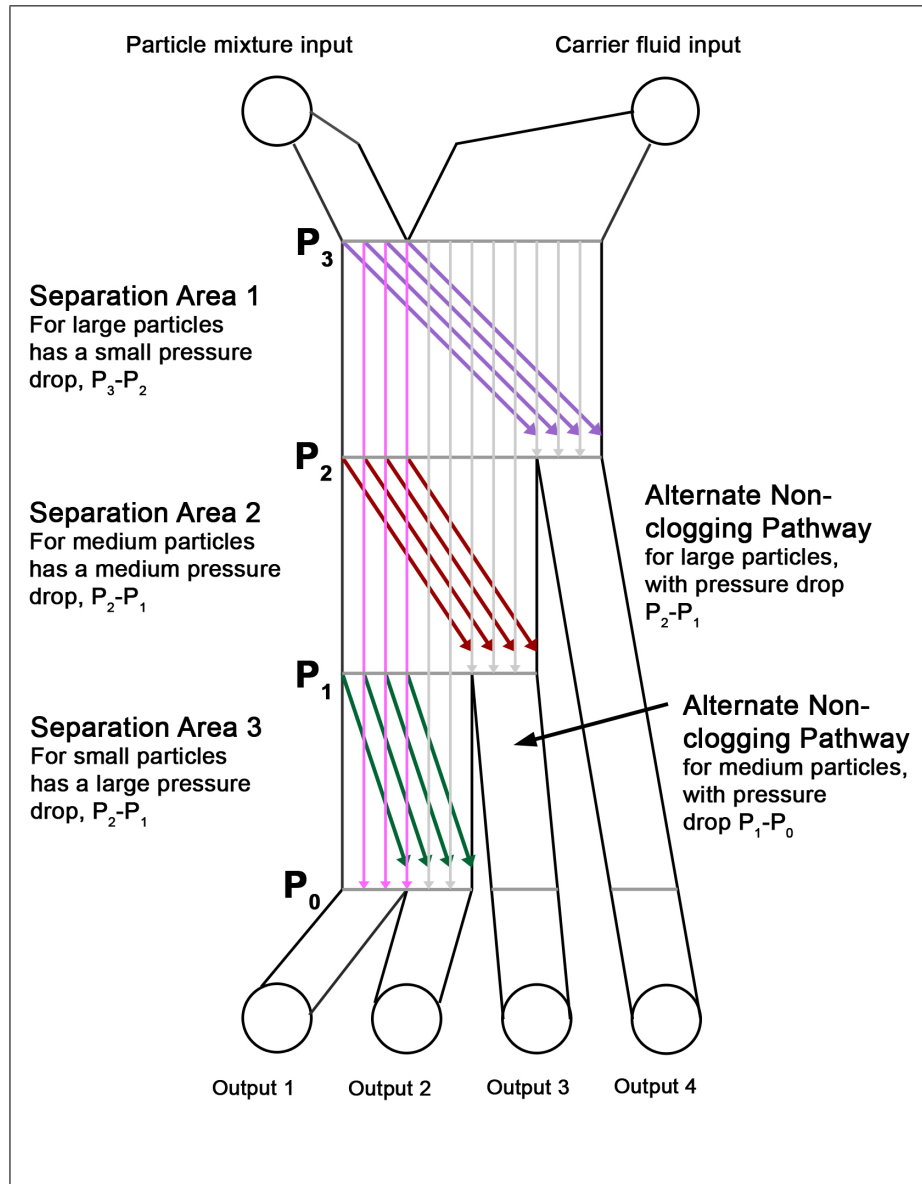
Figure 4.3: Illustration of a device having three cascaded separation areas, each with a decreasing particle separation range. There are alternate non-clogging pathways for particles separated in Areas 1 and 2. By definition the pressure drop over the alternate pathway leading to Output 4 must equal the pressure drop over Separation Areas 2 and 3. The pressure drop over the Alternate pathway leading to Output 3 must equal the pressure drop over Separation Area 3. The differences in feature size in these areas lead to very different resistances per unit width in each section. This can drastically alter the flow profile away from the vertical one that is shown.

This may even result in no separation at all. The following section describes how the alternate non-clogging arrays can affect the flow profile in the separation arrays and how to correct the problem. In general we correct this problem by supplying addition fluid to the alternate paths so that, even though they have low resistance and high velocity, they do not affect the vertical flow in the separation areas.

Design of non-clogging alternate pathways

To cascade multiple bump arrays with decreasing gap sizes it is necessary to provide an alternate non-clogging path for the large, separated particles to follow so that they do not jam or clog the downstream separation arrays. These alternate pathways must collect the separated particles from an upstream section and divert them around the downstream section, without clogging themselves or altering the flow profile in any of the separation arrays. The fluidic resistance per unit width for any collection of paths, a collection of parallel channels for example, depends on the geometry of the channels.

In electrical conduction, resistivity is unaffected by geometry because charge carriers move without coupling due to friction. In fluidic conduction, boundaries slow fluid particles down because of friction, and fluid particles are coupled to one another because of friction. For low Reynolds numbers, the fluid velocity at position $r(x, y)$ in a rectangular pipe of dimension $(h \times w)$ is [48][iii]

$$u(x\big|_0^w, y\big|_0^h) = \left(\frac{4Gh^2}{\mu\pi^3}\right) \sum_{l=0}^{\infty} \frac{(-1)^l}{(2l+1)^3} \times \left[1 - \frac{cosh((2l+1)\pi x/h)}{cosh((2l+1)\pi w/2h)}\right] cos((2l+1)\pi y/h)$$

(4.1)

where G is the pressure drop per unit length and μ is the fluid viscosity. This can be

---

[iii]The cited equation is in error. For equations 12 to 16 in Brody et al. [48] to be consistent (including the well known Darcy and Hele-Shaw results), the power of π should be three not two in the referenced equation.

re-written in terms of the fluidic resistance per unit length, R.

$$R = \frac{G}{\int_0^w \int_0^h u(x,y)\mathrm{d}x\mathrm{d}y} \tag{4.2}$$

When the rectangular channel or pipe becomes tall and narrow, or flat and wide, the resistance per unit length approaches the Hele-Shaw result [48], where h is the smaller dimension:

$$R = \frac{12\mu}{h^3 w} \tag{4.3}$$

When the channel is a square the resistance per unit length has the same form as the Poiseuille result [57] for a cylindrical pipe:

$$R = \frac{28\mu}{\pi d^4} \tag{4.4}$$

This provides two ways to affect the fluidic resistance of a pipe or channel, the diameter (gap) and the length.

The non-clogging pathway here must have a gap of around 20 microns, and the section that separates platelets must have gaps of around 5 microns. This is a large difference in resistivity and, if the tubes were circular, would require a length difference of $(\frac{20}{5})^4 = 256$ times to compensate.

Alternatively we can sometimes control the pressure and flow rate at specific points in the device. We could for example, put the different output ports at different pressures to retard or encourage fluid flow to the correct places, there-bye creating vertical flow in the separation regions. We can also design the device to funnel extra fluid into the low resistance paths to ensure that the appropriate amount of fluid flows into the high resistance paths. This additional fluid flux through a particular path, increases the pressure drop in that path. In my experience, this is the most convenient method for balancing the flow to various paths in order to maintain vertical flow.

To save some length in the device we have designed pathways which run parallel to and maintain constant fluid connection with the separation arrays while not significantly altering the flow profile in the arrays. Figure 4.4 shows a graphical implementation of this idea, where the non-clogging pathway runs parallel to and in constant fluid connection with the separation or bump arrays. The width of the alternate non-clogging pathway is reduced in each section to increase its flow rate and keep the flow profile in the adjacent region vertical. In the actual device design (Fig. 4.6), the chip is much, much longer, accommodating very small values of ϵ.

This non-clogging pathway does not have the same resistance as the separation area that it runs beside, and since it cannot be made any longer than the separation area that runs parallel to it, it carries additional fluid flux, which increases the pressure drop in that area. This solution to the problem of fluidic resistance matching is illustrated in Figure 4.5. It shows simulated flow lines through two regions of different fluidic resistance in constant fluid connection. Fluid prefers to flow in the low resistance area, and will move there when possible. By supplying additional fluid to the low resistance region, the flow profile can be corrected, as in Fig. 4.5B. This figure illustrates the general concept of how to create equivalent pressure drops in the two regions with different features. In the actual device we use an alternate non-clogging path that is not composed of posts, but of a serpentine like pattern (right hand side of Section 2 and 3 in Fig. 4.6) because it has a slightly higher resistance per unit width than the simple post array.

4.3.1   Array design

We use a wide blood injector next to a buffer injector. The blood cells are bumped into the parallel running buffer stream, leaving just the plasma. There are two input connections and two output connections (Fig. 4.6).

The device was fabricated in <100> silicon by standard photolithography and
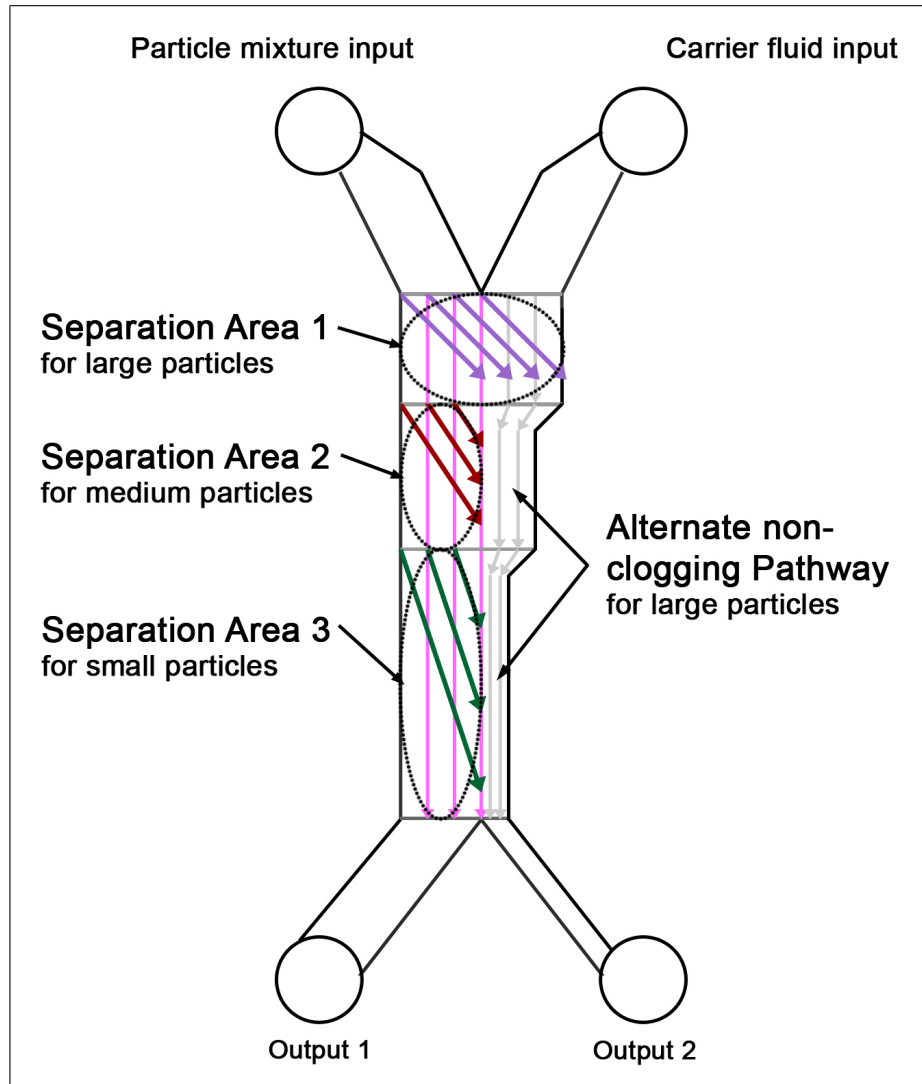
Figure 4.4: Illustration of three cascaded separation areas, each with decreasing particle separation size. The alternate non-clogging pathway runs parallel and adjacent to the last two separation regions. This reduces the length of the device. The width of the non-clogging pathway is reduced at each section to increase the speed in the low resistance non-clogging pathway. This ensures vertical flow in the separation areas.
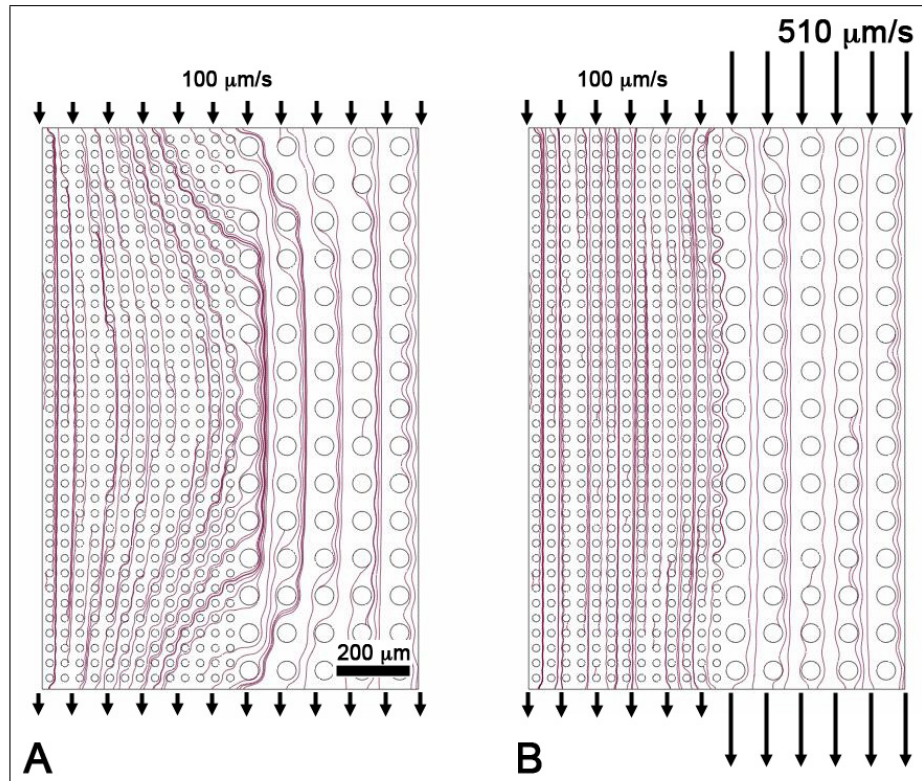
Figure 4.5: Two computer models of fluid flow through adjacent high and low resistance post arrays. The circles are the posts; fluid flows around the posts. The thicker lines are randomly-placed lines of flow. The area on the left of A and B has smaller posts and smaller gaps, giving it a higher resistance per unit width than the area on the right of A and B. In A, the fluid flow is not vertical; fluid moves to the low resistance area when possible. In B, additional fluid is supplied to the low resistance area, preventing lateral flow.

vertical dry etch. The etch was performed by K. J. Morton in the Princeton University Nanostructures Laboratory (courtesy of Prof. S. Y. Chou) using a Bosch® process on an inductively coupled plasma etcher. This device was etched to a depth of 20 microns. Holes were sandblasted through the silicon substrate and the device was sealed with a PDMS-coated glass slide.

Whole blood enters the device on the left and forms a stream that is 500 μm wide; buffer enters the device on the right and forms a stream that is 600 μm wide. The streams flow parallel and experience only diffusional mixing. The cells are "bumped" out of the blood into the parallel stream of buffer. At the end of the device their are two outputs, one to collect the cell-free blood plasma and one to collect the cells and buffer.

The task of bumping the cells into the buffer is performed by three sections of post arrays. The first section is 17.6 mm long, 1100 μm wide, and containts 10-μm diameter posts. The rows of posts have a 16 μm period and the columns of posts have a 30 μm period, with the columns tilted at 2.828^o to the channel walls and the average flow direction. This is a row shift of 0.80 μm. This section is estimated to have a critical particle size of 5 μm.

The second section is 21 mm long and contains two parallel parts; a bump array that is 610 μm wide with an estimated critical particle size of 2 μm on the left and a serpentine pattern that is 300 μm wide on the right. The bump array is composed of 9-μm posts with a row period of 13 μm and a column period of 18 μm. The columns are tilted at 1.725^o to the channel walls and the average flow direction. This is a row shift of 0.40 μm. The average fluid velocity in the serpentine pattern is approximately twice that of the bump array.

The third section is 28.7 mm long and also contains two parallel structures; a 520 μm wide bump array with an estimated critical particle size of 1.5 μm and a 160 μm wide serpentine pattern designed to carry the larger cells that would otherwise jam
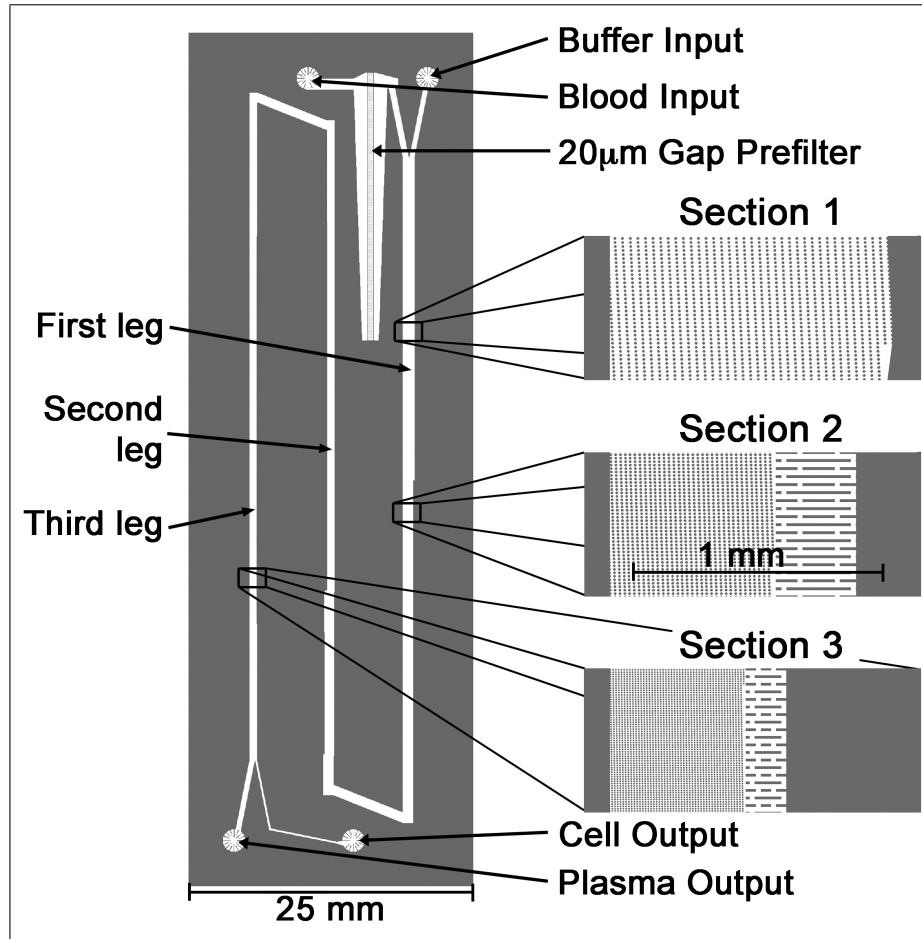
Figure 4.6: Blood flows through a 20 micron gap prefilter, then three successive arrays (§'s 1,2 and 3), with decreasing critical particle size (dimensions in text). Cells are "bumped" from left to right out of the plasma and into the buffer flowing in the serpentine region. Section 1 ends about halfway down the first leg. Section 2 begins in the first leg, is interrupted by the corner, and ends part-way up the second leg. Section 3 extends over about half of the second leg and all of the third leg, with an interruption for a second corner.

Section	Critical Particle Size (μm)	Separates	Viewing Method
1	5	WBCs	Hoechst (blue fluorescence)
2	2	RBCs & platelets	reflection &PE-CD41 fluorescence
3	1.5	remaining platelets	PE-CD41 fluorescence

Table 4.2: Summary of sections in the device and the cells that they primarily separate.

the bump array and accept new cells throughout the length of the section. The bump array uses 6-μm diameter posts with a row period of 9 μm and a column period of 11 μm. The columns are tilted at 0.854^o to the channel walls. This is a row shift of 0.14 μm. The average fluid velocity in the serpentine pattern is three to four times faster than that of the bump array.

At the end of section three the platelets, red blood cells, and white blood cells are all observed to be traveling in the serpentine pattern, completely bathed in buffer, while the blood plasma is still flowing on the left. Table 4.2 shows where certain cell types are separated and how they are viewed.

4.4 Experiment

After assembly the device was soaked overnight in a 2 g/L solution of F108 in DI water to remove any bubbles. Prior to flowing blood, the device was flushed with phosphate-buffered saline (AutoMACS buffer, Miltenyi Biotech, CA) containing BSA, EDTA, and the same concentration of F108. Blood, obtained by finger prick and collected in a EDTA-coated tube, was loaded into the left port of the device. Positive pressure, equally applied to both inputs, was used to drive the fluid. We used either Hoechst 33342 to fluorescently label the white blood cells or antihuman CD41-conjugated phycoerythrin (PE-CD41) to fluorescently label the platelets.

In the first section, white blood cells and a small percentage of red blood cells were
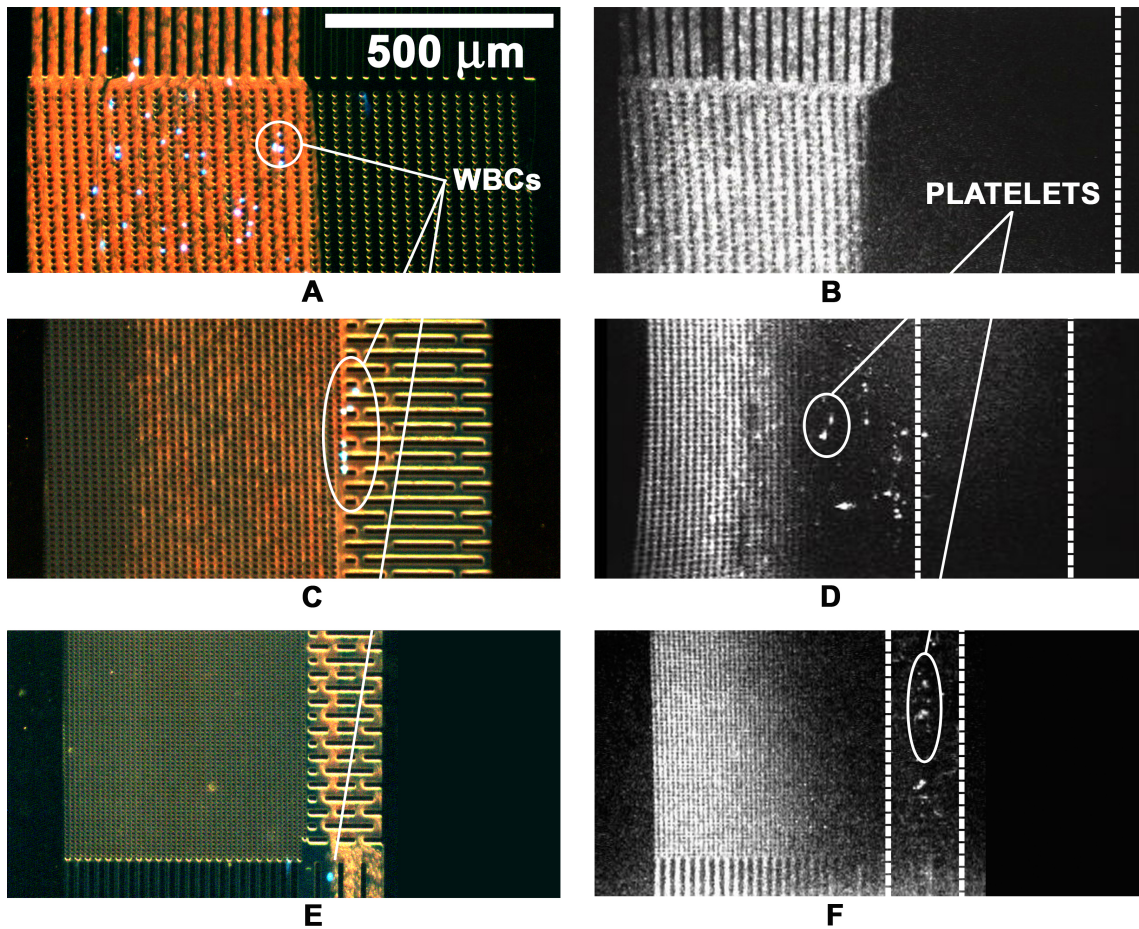
Figure 4.7: Photomicrographs showing whole blood entering the device and exiting the device after being separated into cells and plasma. Whole blood enters the device on the left while phosphate buffered saline enters on the right. Flow is from top to bottom. A: Whole blood with Hoechst 33342 label entering the array. Red blood cells appear red and nucleated cells (white blood cells) are blue. B: Whole blood with an excess of Phycoerythrin-conjugated CD41 antibodies (PE-CD41) entering the array. White areas contain higher concentrations of the fluorescent molecule. C: Whole blood with Hoechst midway through the device. D: Blood with an excess of the platelet label, PE-CD41, midway through the device. E: and F: labeled blood exiting the device. The unbound fluorescent molecules remain on the left and indicate that the liquid portion of the blood has be separated from the cells, while platelets, small white dots and streaks on the right, have been completely bumped into the buffer stream.

observed to travel in the "bump" mode, placing these cells in the buffer stream. Figure 4.7A shows whole blood (red) with fluorescent white blood cells entering section 1. Figure 4.7B shows whole blood with a very high concentration of fluorescent PE-CD41 entering the array. Some PE-CD41 has bound to platelets and some remains in solutions. Most of the fluorescence in Figures 4.7B,D and F is from unbound dye molecules. In the second post array section, most red blood cells and some platelets are observed to travel in the "bump" mode, Fig. 4.7C and D. In the third post array section, the remaining platelets and red blood cells are observed to travel in the "bump" mode. At the end of section 3, all cells have been separated from the plasma and are observed to travel in the serpentine region. Figure 4.7E shows whole blood (red) with fluorescent white blood cells exiting section 3 completely flowing in the serpentine region. Figure 4.7F shows whole blood with fluorescent PE-CD41exiting section 3. The platelets are small white dots and streaks to the right, while unbound, solubilized, PE-CD41 remains in the bump array. The experiment was also performed with a lower concentration of PE-CD41. No platelets were ever observed to travel in the bump array at the end of section 3.[iv] Therefore, experimentally we have performed the first demonstration of a continuous blood filter that removes all of the cells from the plasma.

4.4.1 Future work and loose ends

The objective of this device was to produce cell-free plasma and plasma-free cells. We have shown this through microscopy, but we have not done any analysis of the output products. This is mostly due to hubris, but partly due to errors, made in the design, that resulted in the plasma and cell collection channels to be miss-aligned with the plasma's and cell's actual positions. The first error was failing to account for the

---

[iv]Later work, (Ch. 6), informed us that other preparations of blood produce platelets that are smaller than those observed here and it is unclear if this device would remove all platelets from blood taken using different anticoagulants.

reduction in width/volume of the blood stream experienced after removing the cells from the plasma stream, and similarly, the increase in width/volume of the buffer stream after accepting the cells. Since blood is about one half cells by volume, once the cells are removed the amount of "stuff" left over is significantly reduced. Instead of inputing an equal amount of blood and buffer, I should have input 2 parts blood, and one part buffer, resulting in an output of 1 part plasma and two parts cell-buffer mixture.

The second error, visible in Figure 4.7F, was providing too much resistance in the plasma output channels. In Figure 4.7F, the edge of the dye stream is not vertical, but curves left to right. This is because too much liquid is flowing into the cell-buffer output. Either increasing the width of the plasma output channels or decreasing the width of the cell-buffer output channels by a small amount would correct this problem.

4.5 Limits to pure-plasma extraction resulting from diffusion

In this device, a wide stream of blood plasma flows parallel and adjacent to a wide stream of buffer. The plasma contains ions and molecules that will diffuse into the buffer and vice versa, Figure 4.8. If the plasma is to be used for diagnostic purposes, we must understand what changes occur in the plasma during the separation process and how to minimize them. A thorough study of this effect would involve a professional analysis of the plasma produced by conventional centrifugation and by the microfluidic device. We can estimate the degree of contamination by imaging the diffusion of fluorescent dyes. We do this by adding fluorescent dye to one side of the device and imaging it downstream, thereby tracking the positions of molecules of known molecular weight.
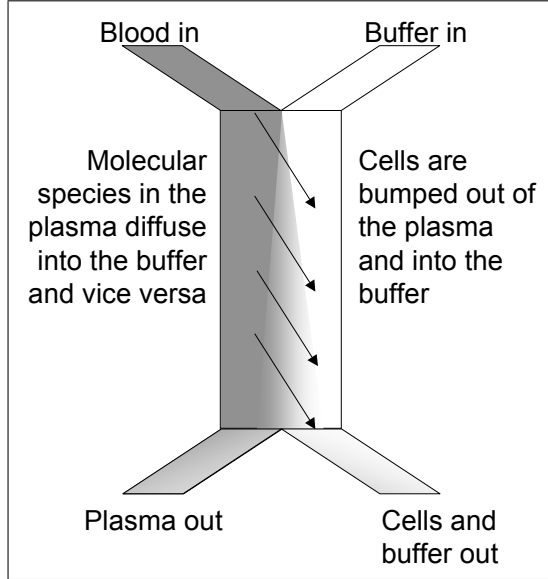
Figure 4.8: Simplified schematic of the cell separation device, where blood enters on the left and buffer on the right. While cells are bumped from left to right, diffusion between the two liquids occurs in both directions, and ideally the "boundary" between the two does not move laterally. The gray and white boundary blurs with time and distance into the chip indicating diffusional mixing of the two liquids.

The diffusion constant for a particle that is more than its own radius, a, away from a wall is

$$D = \frac{k_B T}{6\pi\eta a}. \tag{4.5}$$

The fluid viscosity is η and T is the temperature. A one-dimensional cloud of non-interacting particles will broaden as the square root of time, that is, the change in the standard deviation of the distribution of particles is given by $\Delta\sigma = \sqrt{2D\Delta t}$. The diffusion constant for a 1-micron particle is approximately 0.5 μm^2/s, so a collection of 1 micron particles will spread by 1 micron in the first second and about 3 microns in the first 10 seconds.

In Figures 4.7 B, D and F, a fluorescent dye was added to the blood to demonstrate the molecular species were separated from the blood cells. Here we repeat this experiment with a few details changed. We use dye mixed with water, not mixed with blood, because the red blood cells absorb light and affect the fluorescent intensity in their vicinity. Secondly we inject dye from the right hand side because of the 20 micron gap prefilter (Fig. 4.6). When dye is injected from the left some of it diffuses into the lower portion of the prefilter, this decreases the concentration of the dye that flows at the left most side of the device.

At the beginning of the 1st section the concentration profile of dye is a step function, $C = 0$ for $x < 0$, and $C = C_o$ for $x > 0$. The position, $x = 0$ is 500 microns from the left edge of the device, and for simplicity, measurements are taken at the end of the first section before there are any changes in the width of the device or in the speed of adjacent sections..

Fick's second equation (Eq. 4.6), states that the rate change in concentration, $C(x, t)$, is proportional to the diffusion constant D and the curvature of the concentration profile [58].

$$\frac{\partial C}{\partial t} = D \frac{\partial^2 C}{\partial^2 x} \tag{4.6}$$

An exact solution to this problem can easily be found if there are no other boundaries or obstacles to the diffusing species, that is, the right and left sides of the device extend to $\pm$ infinity. This is an acceptable approximation for flow in the microfluidic device if the concentration at the left and right edges of the chip remains approximately equal to 0 and C_o, respectively. This is true when small amounts of diffusional mixing occur. The solution to Equation 4.6 under these boundary conditions is

$$C(x, t) = \frac{C_0}{2} \left(1 + \mathrm{erf} \frac{x}{\sqrt{4Dt}} \right), \tag{4.7}$$

where erf is the error function.

In this experiment we flow dye in place of the blood and record the brightness of the fluorescent dye stream at the end of section 1. We record images at three different speeds and fit Equation 4.7 to the shape of the brightness histogram by adjusting: 1) the diffusion constant for the dye molecule, 2) the initial concentration, C_o and, 3) the zero position for each run. The same diffusion constant is used for all runs using the same dye. The incoming $x = 0$ position has some dependence ($\pm 50 \mu$m) on speed, this may have been due to small air leaks in the air pressure connections. To compensate for this I have shifted the actual data a small amount left or right to

improve the fit. The brightness of the fluorescent dye is assumed to be proportional to the concentration of dye molecules.

Figure 4.9 shows the brightness histograms for two fluorescent molecules at the end of section 1 at three different speeds. The fit to each histogram is also plotted (smooth lines). We fit the curve with Equation 4.7, where t is the the distance through the chip divided by the average fluid velocity. The lateral position is x. Section 1 is 17.65 mm long, and average fluid speed is 120 μm/s per psi. For example, at 4 psi it takes $\frac{17650}{120 \times 4} = 37$ seconds to flow across section 1. The fit shown in Figure 4.9A was achieved with a diffusion constant of 3×10^{-10} m^2/s. The fit shown in Figure 4.9B was achieved with a diffusion constant of 3×10^{-11} m^2/s. The following figure compares these measured values of diffusion constants to others species with known diffusion constants. Due to the small size of the molecules (~ 1 nm) relative to the channel depth and gap sizes ($\sim 20\mu$m), we have ignored the effect of the surfaces on diffusion [59].

Figure 4.10 shows the diffusion constant versus the inverse of the cube root of the molecular weight. The chart includes the two molecules that we measured, PE-CD41 and Alexa$^{\text{TM}}$-488 maleimide (Invitrogen.com), shown in black. A few other chemical species for whom D has been measured by others are shown in grey. The diffusion constant is inversely proportional to particle/molecular diameter, so if we assume a constant density for proteins of 1.4 g/mL [60] and a circular shape, it is linear with (molecularweight)$^{-1/3}$. This prediction is also plotted in Figure 4.10. The measurements of diffusion constant are in good agreement with the prediction based on molecular weight and other measurements.

We can now answer the question, "How contaminated is the plasma?" We create curves, similar to figure 4.9 for an arbitrary diffusion constant and time, then ask how much, as a percentage, of the incoming species has crossed into the adjacent stream, i.e. crossed the $x = 0$ point. This number is plotted as a function of the flow speed in
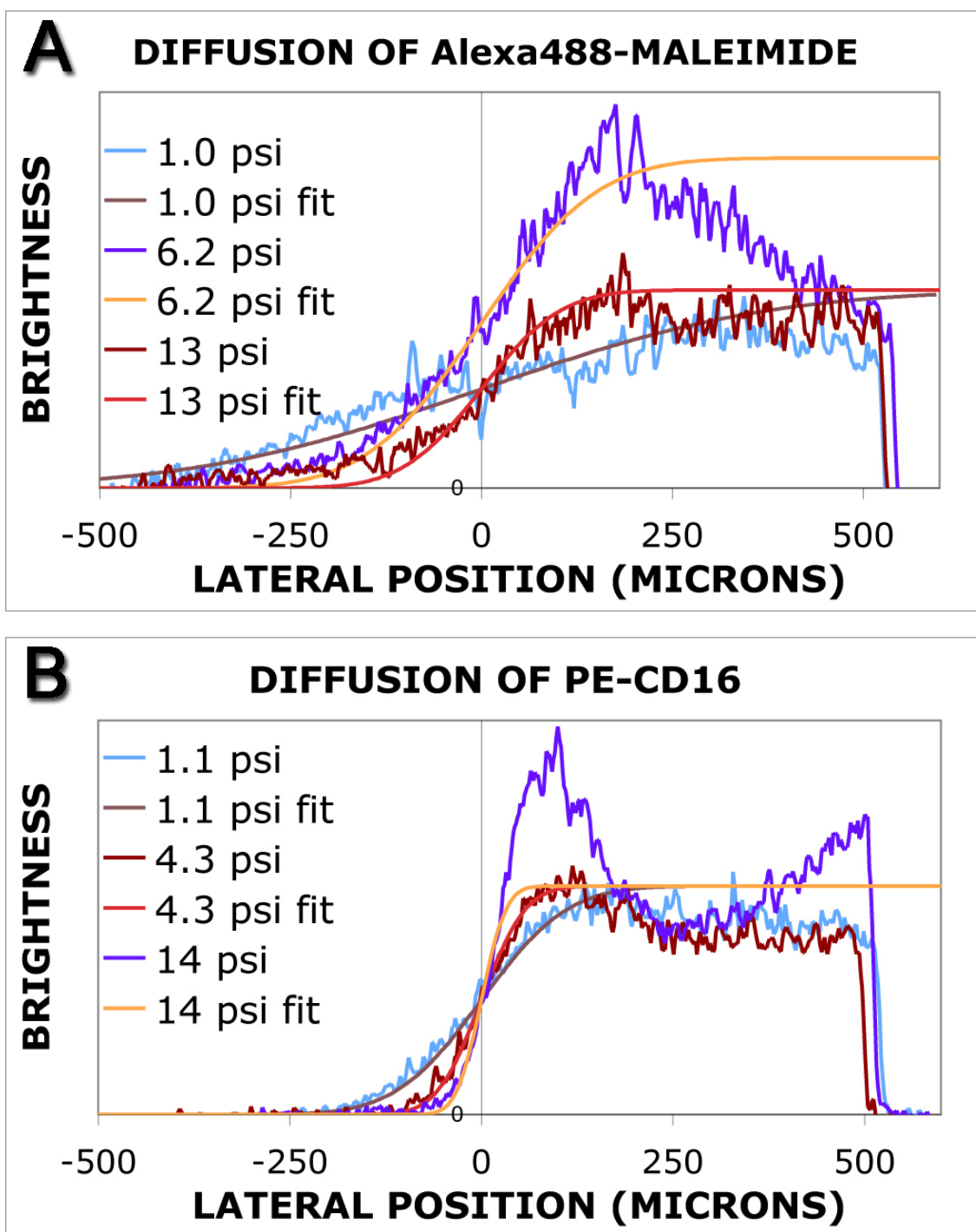
Figure 4.9: Brightness histograms of two dye species after flowing through section 1 of the device at various speeds. The fluid velocity is 120 μm/s per psi. A: Alexa488-Maleimide has a molecular weight of 721 g/mol. B: PE-CD16 has a molecular weight of 150,000 g/mol.
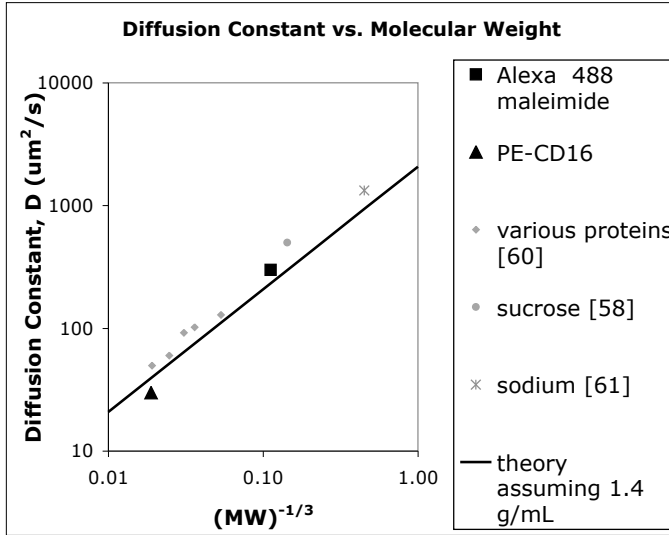
Figure 4.10: Measured [58,60,61] and predicted diffusion constants vs molecular weight.

Figure 4.11. Analytically this can be done by integrating Equation 4.7 from negative infinity to zero.

$$\int_{-\infty}^{0} C(x,t) = C_o \sqrt{\frac{Dt}{\pi}}. \tag{4.8}$$

We can substitute t with L/v where L is the total length of the separation arrays, 10.4 cm, and v is the average fluid velocity. Dividing this by the total amount of species in the blood, $C_o \times 500 \mu m$, gives the fraction that has diffused into the buffer.

Figure 4.11 shows this fraction versus the average speed for various chemicals and diffusion constants. A much larger fraction of smaller species diffuse out because they have a larger diffusion constant. The model predicts that 5% of hemoglobin would be lost at 10 mm/s, and at least 20% of small salts like sodium would diffuse into the buffer stream. For this device, an average flow speed of 10 mm/s would require approximately 50 psi (~3 bar) of positive pressure. The purity of the collected blood plasma can be improved by adjusting the fraction of flow that goes to the two output ports. The plasma on the left-most side of the device will have experienced less mixing with the buffer, so there is a trade off between the amount of plasma that is recovered and the purity of the plasma. Furthermore, one should design devices so that the buffer stream is as narrow as possible to limit the amount of chemical species than

Figure 4.11: Fraction, by Equation 4.8, of total chemical species that will diffuse into the buffer stream from a 500-micron-wide injector, running parallel for 10.4 cm, as in the device described here.

can diffuse into the plasma.

4.6   Volume Flow Rate

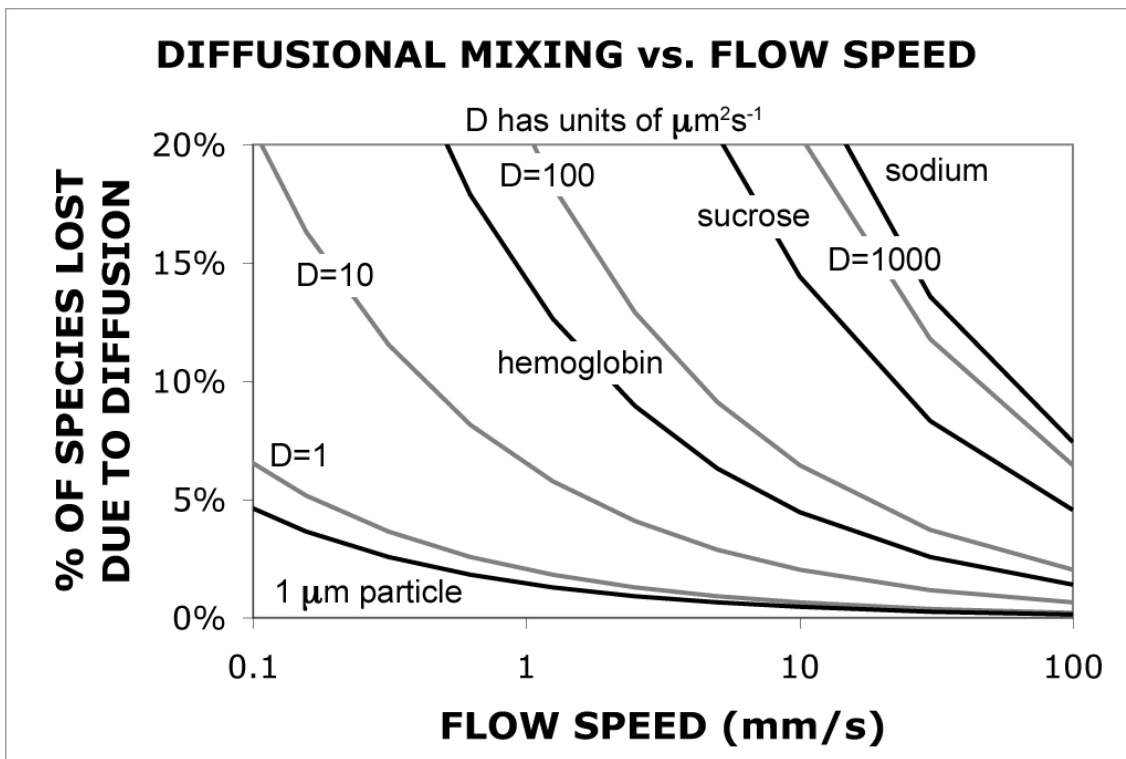A limit to the flow speed is eventually reached due to shear forces. Shear is the gradient of velocity, and can deform and destroy cells. Normal blood flow experiences shear rates of 50 to 2,000 s^{-1} [62–64]. Holme et al. [63] reported shear-induced platelet activation at 10,500 s^{-1}, while Markou et al. [64] reported no activation at shear levels up to 280,000 s^{-1}, but did begin to see cell lysis beyond this shear.

At 5 psi, this device separates 0.25 μl per minute. The speed in the final serpentine region is approximately 2000 μm/s, corresponding to a shear rate 200 s^{-1}. A very rough estimate of the shear rate is arrived at by dividing the average speed by one half of the channel dimension, i.e. the velocity changes from 0 to v_{ave} in half of the channel width. In the bump array portion of the section 3, were the gap is 5 microns, the speed is approximately 600 μm/s, also corresponding to a shear rate of 200 s^{-1}. The device de-laminates, that is, the silicon and PDMS layers separate at approximately 70 psi, though the bond strength can be increased significantly by oxygen plasma treating the PDMS prior to sealing. This suggests that at an operating pressure of 50 psi, the blood would be exposed to roughly physiological levels of shear, and 2.5μl per minute of blood could be separated. At that rate it would take 111 days to process one 400-ml bag of blood.

It is straightforward to further increase the throughput by etching 10 times deeper and running 10 devices in parallel, and since others have shown that blood is not damaged by shear that greatly exceeds physiological levels, the device could possibly be run another factor of 5 faster. Applying all of these, the time to process one 400-ml bag of blood drops to 5 hours.

4.7 Summary

Blood separation by centrifugation is, next to microscopic observation, perhaps the most general hematological procedure. Any sophisticated blood analysis chip must be capable of sorting blood cells in a similar way. In this chapter we have demonstrated the first continuous-operation blood filter that removes all cells. In doing so we have demonstrated how multiple "bump" arrays with different gap sizes can be linked together to separate cells over a wide range of sizes. The device shows great promise as a method for on-chip blood separation. However in its current design, the diffusion of species between blood and buffer streams is a significant effect, with greater loss of lower molecular weight species.

Chapter 5

DLD for Profiling the Size of Large Blood Cells

5.1 Introduction

The deterministic lateral displacement or "bump" method provides a convenient way to measure the size of cells. Cell size is one of many parameters that can be used to identify cells. This chapter describes a microfluidic device used to measure cell size and compares it to measurements of cell size made using a conventional flow cytometer. Flow cytometry is an important analysis and separation tool in research and clinical settings because it is flexible, rapid, real-time and multi-parameter.

Flow cytometers optically probe a hydrodynamic jet of cells one cell at a time as they pass through the focal point of a laser beam. An array of sensitive and fast opto-electric transducers record the the intensity of: 1) light scattered at low angles to the incident beam, forward scatter, 2) light scattered at $\sim 90°$ to the incident beam, side scatter, 3) light emitted at $\sim 90°$ to the incident beam, but with a longer wavelength, i.e. fluorescence. Basic flow cytometers often have the optical components to capture the fluorescence from three different fluorescent dyes simultaneously. More advanced

flow cytometers can have multiple lasers and more than 10 different fluorescence channels. Cells or events are measured one at a time, currently as rapidly as 15,000 events per second, with volume flow rates of 10's to 100's of μl per minute, depending on the cell density.

Separation of cells is performed downstream of the optical interrogation point by breaking the hydrodynamic jet into individual droplets which then pass though a pair of electrically charged plates. After the optical interrogation, the computer in the flow cytometer analyzes the parameters of the event/cell and decides how to charge the nozzle from which the droplet breaks free. The transition from continuous fluid stream, where the optical interrogation takes place, to the droplet stream is repeatable. This allows for a know time delay between analysis and droplet formation, during which the computer can decide how to charge the nozzle. The charged droplet will fall at an angle through charged plates and land in a different container than uncharged droplets. Droplets can be charged to various values, positive and negative to allow for collection in numerous containers

Microfluidic platforms for cell separation have not currently found much use, but there is a definite trend toward smaller machines and a need for affordable and specialized tools [65,66]. Microfluidic-based systems present a few advantages, including better optical coupling, reduced size, and disposability of cell-handling components, not to mention the potential for new science. Microfluidics may also be the best approach for building inexpensive "personal flow cytometers".

In flow cytometry the magnitude of light scattered at low angles is called forward scatter. It is the closest thing to a size measurement typically available. Performance is generally very good for particles of similar structure, having a linear response to diameter over a wide range of particle sizes. The forward scatter signal is however, strongly dependent on particle structures such as the absorbency of the material, surface texture and internal granularity. Forward scatter nevertheless gives reproducible

patterns that are essential for identification of cells.

This chapter describes a method for determining the diameter of particles based on a recently published microfluidic method for particle separation [5]. As described in Chapter 3 the method is deterministic and bi-modal, that is, for a certain array of posts, particles travel in one of two possible modes which are separated by a small angle. Particles less than a critical diameter follow the fluid flow direction. Particles larger than a critical diameter follow the direction of the columns formed by the array of posts. The critical particle diameter is proportional to the gap between adjacent posts in a row, and is also a complex function of the columnar slope, (Fig. 3.4).

5.2   Device design

The device used here for blood cell sizing has eleven arrays fabricated in series on a single chip to continuously fractionate an narrow stream of blood. In the first array, two possible paths exist, one vertical path for the smallest particles and one, for larger particles, that travels away from the other path at a small angle. In the next array the first stream is unaffected, but the later path bifurcates into two new paths: one vertical paths for smaller particles and one for larger particles that continue to move away from the others at a small angle. So after 2 sections, there are ideally 3 possible paths. After eleven arrays there are ideally twelve different, laterally separated, streams that particles could follow, containing particles with increasing size from left to right. Diffusion of particles and imperfections in the array blur these streams into a nearly continuous distribution of sizes.

The device fits on a standard 25×75 mm glass slide, having two input ports (one for buffer and one for blood) and two output ports, the left half of the device going to one port and the right half going to the other port. Blood is injected in a focussed ($<20\mu$m wide) stream, 115 μm from the left device wall. The array specifics

ϵ	Post Diameter	Gap	Length of Section	Lateral Displacement
1/100	22	23	13500	135
1/50	22	23	4500	90
1/25	22	23	2249	90
1/22	22	23	1980	90
1/18	22	23	1620	90
1/15	22	23	1350	90
1/12	22	23	1080	90
1/10	22	23	900	90
1/10	19	26	899	90
1/12	56	34	1081	90
1/9	56	34	811	90

Table 5.1: Device specifics as in L-Edit (Tanner EDA, CA USA) mask file "WBC-histogramer_V1_2.tdb". The separation column is 1300 μm wide. Dimensions in the table are microns.

are described in Table 5.1. The arrays are rhombic, that is, the rows are always horizontal and orthogonal to the average flow. The last row of posts within each section partially overlaps with the first row of posts in the next section, generating an elliptical-like post that makes finding the section boundaries easier.

Devices were molded in PDMS (GE Silicones, Wilton CT, USA) from 20- to 30-μm deep etched silicon master molds and sealed to fluorosilane-coated silicon wafer pieces. The gaps between the posts are no smaller than 20 microns. AutoMACS^{TM} buffer (Miltenyi Bioech, Auburn CA, USA) with 2 g/l pluronic F108NF (BASF, Mount Olive NJ, USA) was used as the running buffer. A high pressure mercury lamp was used as the excitation light source in all experiments. Fluorescence intensity histograms for bead populations were acquired using a Retiga 1300 intensified camera (Q-Imaging, Burnaby BC, Canada) and a Nikon Diaphot 300 inverted epi-fluorescent microscope.

Figure 5.1 demonstrates the actual performance of the device using fluorescent 2.3-, 6-, 8.4-, 10.1-, and 15.0-micron diameter polystyrene beads. The figure plots the fluorescence intensity versus position on a single graph (each bead size measured independently in time lapse images). Particles less than 5 microns in diameter experience no lateral displacement and exit the device directly downstream of the particle

injection point, 100 microns from the left device wall. Particles greater than or equal to 18 microns are displaced in every section and exit the device ∼1160 microns from the left device wall. Thus from the output position of a cell or particle we can infer its size. The exit positions of the bead populations are used to calibrate the device for measuring cell sizes. Figure 5.2 shows the calibration between particle size and exit position obtained using the polystyrene beads.

The 2.3 and 10.1-micron beads came from Duke Scientific (Palo Alto, CA, USA), the 6-micron beads from BD (Franklin Lakes, NJ USA) and the 8.4- and 15-um beads from Bangs Laboratories (Fishers, IN, USA). Cell histograms were created by first recording video of the cell streaks on a Sony DV-G1000 miniDV recorder from a Hamamatsu silicon intensified target camera, and then reviewing the tape and recording the cell's positions.

5.3 Experiments and results

5.3.1 Size measurements of different cell types

To evaluate the performance of the microfluidic cell sizer we analyzed three cell groups: $CD4^+$ T-lymphocytes and $CD14^+$ monocytes in whole human blood, and a $CD4^+$ leukemic cell line known to be abnormally large, J45.01 lymphocytes from the American Type Culture Collection (ATTCC number CRL-1990). The blood was collected from a finger prick into an EDTA-coated collection tube. The J45 cells were grown in RPMI 1640 containing 10% fetal bovine serum and 1% penicillin-streptomycin (all from SigmaAldrich.com), at 37 ^{o}C under 5% CO_2. All cells were labeled with phycoerythrin (PE)-conjugated antibodies. Samples with different labels were run separately. They were run through a device which is five centimeters long, at an average speed of 1 millimeter per second at a concentration of approximately 500 WBCs per microliter. PE-anti-CD4 was used to label the J45 cells.

NORMALIZED BRIGHTNESS FOR BEAD POPULATIONS AT THE END OF THE MICROFLUIDIC DEVICE

2.3 6 8.4 10.1 15 μm Nominal bead diameter

Fit to data

Manufacturer specified

No displacement

EXIT POSITION (MICRONS)

Figure 5.1: Normalized fluorescence intensity versus position at the end of the device for spherical polystyrene beads of sizes 2.3, 6, 8.4, 10.1 and 15 microns (specified by manufacturer). At the end of the device, the 2.3 micron beads (black) have experienced no lateral displacement while the 15 micron beads (orange) have experienced the most lateral displacement. The observed standard deviation for the displaced bead populations are shown graphically in gray. The manufacturer's size variations for the displaced beads are shown in black when available. The fine structure in the peak shapes are caused by post-particle interactions upstream of the image acquisition point.

MICROFLUIDIC DEVICE CALIBRATION

PARTICLE DIAMETER (MICRONS)

EXIT POSITION (MICRONS)

Figure 5.2: Plot of bead diameter versus exit position. This segmented line is used to calculate the diameter of cells based on their exit position in the microfluidic device. Horizontal error bars are one standard deviation left and right, as determined by fitting a gaussian to the fluorescence intensity profiles shown in Figure 5.1. Vertical error bars are determined from the coefficient of variation specified by the manufacturer.
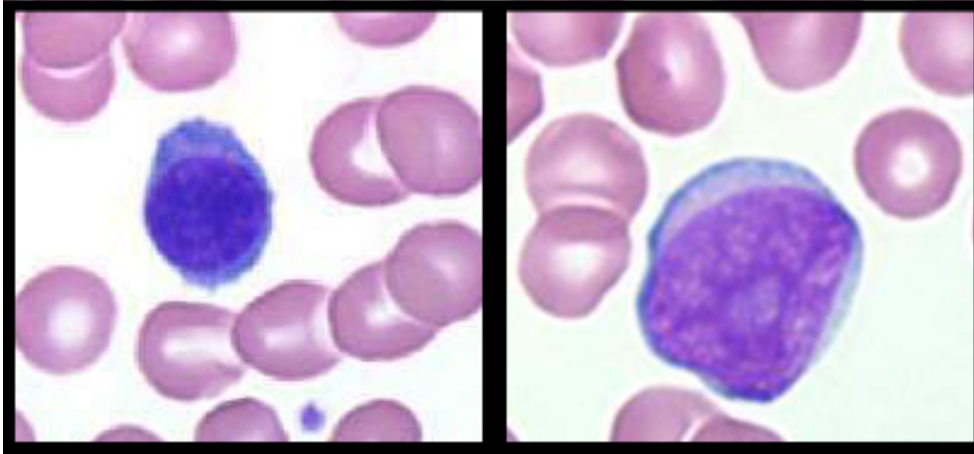
Figure 5.3: LEFT: image of a normal lymphocyte. RIGHT: image of myeloblast produced in acute myelocytic leukemia. The leukemic cell is approximately 60% larger than the healthy cell. The scale can be inferred from the red blood cells, which are 7 to 8 microns in diameter. Source: Wadsworth Center of the NYSDoH, viewed 6/28/07 at http://www.wadsworth.org/chemheme/heme/microscope/lymphocytes.htm and http://www.wadsworth.org/chemheme/heme/microscope/aml.htm.

All cells exit the device through one of 27 possible exit channels, the histograms presented are created by counting fluorescent cells as they pass through these channels. How these channels are connected to output ports depends on the application. For example if channels 20 to 27 (885 to 1200 microns) were connected to one output, we would expect 73% of J45 cells and 0.2% of CD4$^+$ cells to be collected there, a 365 fold enrichment of J45 cells over normal CD4$^+$ cells. Davis et. al. [47], using a similar microfluidic device with 5 output channels, analyzed the cellular output using a flow cytometer. They showed that monocytes and lymphocytes could be separated from 99% of red blood cells.

The goal of this chapter is not to separate the red blood cells from other cells, as in Davis et al. [47]. It is to make histograms of the white blood cells, with the goal of being able to detect abnormally large cells which occur in leukemia and in response to certain bacterial toxins. Figure 5.3 shows an image of a normal lymphocyte and a myeloblast (an abnormal lymphocyte produced in a patient with acute myelocytic leukemia). The myeloblast shown is approximately 1.6 times larger (linear dimension)

than the healthy lymphocyte shown.

Figure 5.4A shows that the three cell populations form clearly resolvable peaks with very little overlap between the J45 leukemic cells and the healthy CD4$^+$ T-lymphocytes. There are three peaks; the CD4$^+$ T-cells are the least displaced, the J45 cells are the most displaced and the CD14$^+$ monocytes are in between. Comparing the results from the microfluidic device to the forward scatter values from conventional flow cytometry, Figure 5.4B, the overall shapes and widths of the peaks in Figure 5.4A and Figure 5.4B are remarkably similar. Error bars on the plot in Figure 5.4A represent the standard deviation observed during experiments on 6 different devices, using 3 different blood samples. The J45 cells were taken from culture, on three different occasions, approximately 2 days after diluting culture with new medium. Approximately 1200 cells were counted in total for each cell type.[i]

We calculate a mean cell diameter of 8.5 microns for the CD4$^+$ cells and 10.4 microns for the CD14$^+$ cells. Of the CD4$^+$ T-cells, 0.2% were larger than 12 microns (exit at $> 800 \mu$m). These larger cells may be activated lymphocytes, background events caused by particles in the running buffer or some other abnormal cell. The peak of the J45 cells lies beyond the last experimental point in Figure 5.2 (15.0 μm), so we are unable to calculate the mean size.

It is important to note that red blood cells were not lysed prior to running in the microfluidic device as is typically required for flow cytometry. Red blood cells can occlude the optical detection processes in a flow cytometer, therefore they are usually selectively lysed prior to running. The red blood cells nearly all behave as particles with diameters less than 5 microns so they exit the device with no displacement and are thus spatially separated from most white blood cells. The ease with which most

---

[i]The blood used for the CD4 and CD14 comparison in the microfluidic device was obtained by a finger prick of the first author. Blood used for flow cytometry and SEB tests was obtained by venous blood draw at the Wadsworth Center of the New York State Department of Health. The PE-anti-CD4 (OKT4 clone) and the PE-anti-CD14 (61D3 clone) antibodies were from eBioscience, San Diego CA, USA.
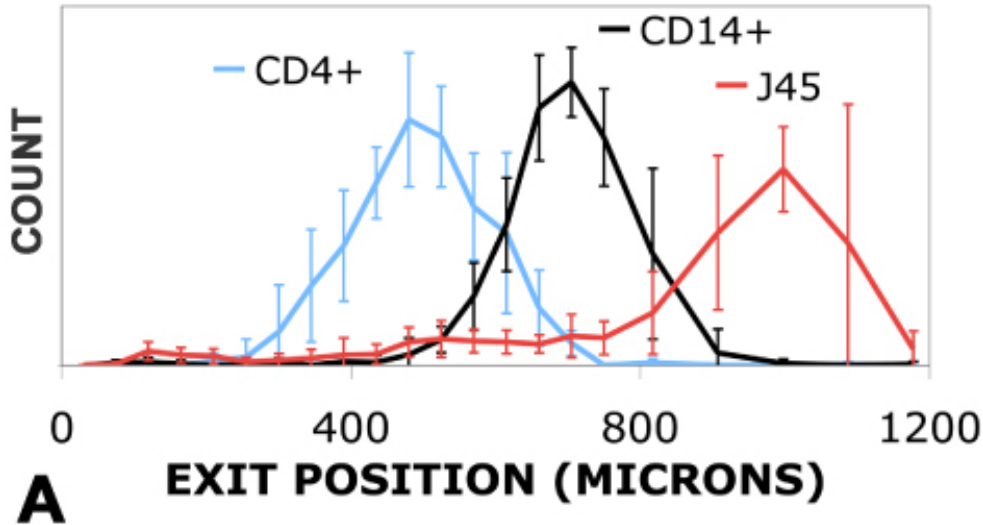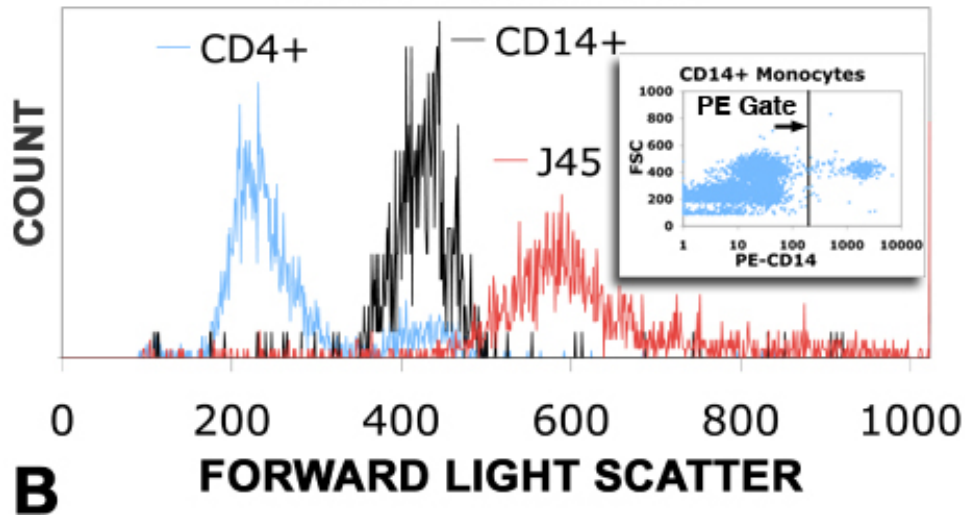
Figure 5.4: Comparison of size measurements for three cell types from the experimental device (A) and conventional flow cytometry (B). CD4+ (blue) and CD14+ (black) cells are from whole blood, CD4+ labeled J45 T-lymphocytes (red) from cell culture. (**A**) The error bars express the standard deviation observed between six independent tests. (**B**) The forward scatter value for only those cells whose PE fluorescence value was over 200 (of 1024) are included in the plot. The inset figure in (B) shows a typical plot of forward scatter (FSC) vs fluorescence, PE-CD14 in this case. The PE-gate at 200 is shown as a vertical black line.

of the red blood cells can be separated from the white blood cells suggests that the technology could be incorporated into the flow cell in conventional flow cytometry. This would save time and may preserve the natural state of the white blood cells better than with lysing which exposes them to harsh conditions.

Statistical analysis.

The count of CD4$^+$ cells versus position fit a Gaussian distribution with a mean of 498 and standard deviation of 138 microns, $R^2 = 0.991$. The count of CD14$^+$ cells versus position fit a Gaussian distribution with a mean of 704 and a standard deviation of 113 microns, $R^2 = 0.996$. The J45 cells fit a Gaussian distribution with a mean of 985 with a standard deviation of 145 microns. Using this information and the curve shown in Figure 5.2 we were able to calculate mean cell diameter for the CD4$^+$ and CD14$^+$ cells given earlier.

We observed a background of 0.07 events per minute evenly distributed throughout the fluid flow area. These are believed to be fluorescent particles in the sheath/buffer fluid. This background accounts for half of the events observed in the CD4+ distribution above 12 microns in diameter. If this data were taken to be the standard then we could detect abnormally large lymphocytes when present at more than one in 500 CD4$^+$ cells.

5.3.2   Potential use in detecting leukemia

Leukemia involves the abnormal proliferation of hemopoietic cells (blood stem cells). These cells normally reside in the bone marrow and other organs, but in leukemia they appear in the blood. Enriching or concentrating these cells would make early detection of this disease easier. Using the microfluidic device, lymphoid leukemic cells similar to the J45 cells used here could be detected, based on our current background counts, when present at more than one cell per 500 CD4$^+$ lymphocytes. Leukemic

cells account for a growing number of the circulating cells as the disease progresses and can reach 10% of the lymphocyte population. The detection limit is set by the background of $CD4^+$ events that occur where large objects ($> 12\mu$m) normally occur. Further experiments with an automated data collection system would provide a clearer picture of what the normal frequency of large lymphpocytes is.

5.3.3 Size response to SEB stimulation

As a further evaluation of the device, we show that the device is sensitive to changes in lymphocyte size caused by exposure to an activating toxin. When exposed to a stimulating antigen, a portion of competent lymphocytes dedifferentiate into more immature forms and proliferate mitotically. The more immature form is called a transformed or activated lymphocyte (or a lymphoblast) and is larger in diameter than a normal lymphocyte by a few microns. After proliferation these cells mature into normal lymphocytes. The observation of an elevated number of large lymphocytes is evidence of lymphocyte blasting [44], which is usually the stage preceding mitosis and could be potential evidence of malignant transformation.

Staphylococcal enterotoxin B (SEB) (Sigma Aldrich) is a bacterial superantigen protein that causes activation of lymphocytes in a large portion of people. Clinical symptoms depend on the route of exposure but ingestion of SEB typically causes food poisoning within 1 to 6 hours. Whole venous blood (100microL Na-Heparin) diluted with minimal essential medium (100 μl) was incubated with 1 μg SEB at 37°C in 7% CO_2, 5% O_2 for 24 hrs.

Figure 5.5 shows normalized size histograms comparing the SEB and control sample analyzed in the microfluidic device (a, c), and by flow cytometry (b, d). A qualitatively similar increase in the proportion of large lymphocytes in the SEB sample can be seen with each method. Here we are looking at the small increase in height of the histogram on the right shoulder and tail of the peak. To quantify the difference
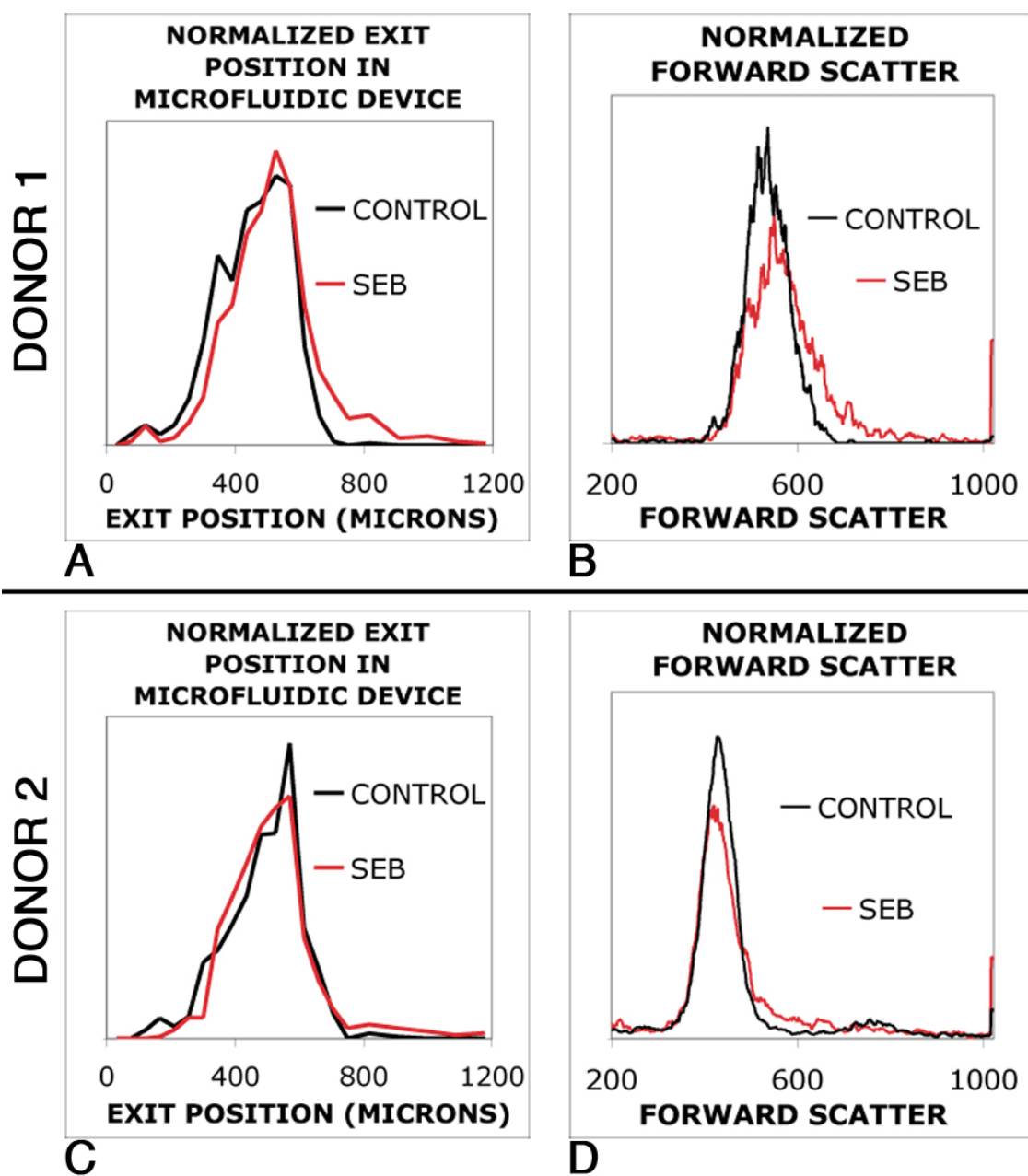
Figure 5.5: Comparison of size measurements for blood incubated with the activating toxin SEB using the microfluidic device and conventional flow cytometry. For each donor and with each method, the SEB sample (red) has a higher proportion of moderately larger cells compared to the control (black). In (A) the number of cells beyond the down-sloping crossover point increased by 2.6 times in the SEB stimulated sample. For the sample sample measured by flow cytometry (B) the increase was 2.7 times. In (C) and (D) the fraction of cells to the right of the crossover points increased by 2.5 and 1.5 times, respectively.

Figure 5.5 panel	Donor	Measurement method	×-over point	Increase in large cells
A	1	microfluidic	615 μm	$\frac{20\%}{7.7\%} = 2.6$
B	1	flow cytometry	584	$\frac{41\%}{15\%} = 2.7$
C	2	microfluidic	705 μm	$\frac{5.7\%}{2.3\%} = 2.5$
D	2	flow cytometry	483	$\frac{26\%}{17\%} = 1.5$

Table 5.2: Summary of Figure 5.5 and comparison of the measured increase in the fraction of large cells.

we can compare the results by taking the fraction of the curve that lies to the right of the cross-over point in each case. The cross-over is the point on the right shoulder of the peak where the SEB value becomes greater than the CONTROL value. In Figure 5.5B this is clear and occurs at a forward scatter value of 584. In A, C the cross-over points are at 615 and 705 μm respectively, and in D the cross-over point occurs at a forward scatter value of 483. For donor 1 we observe a 2.6 fold increase in the number of cells beyond the cross-over using the microfluidic device and a 2.7 fold increase using the flow cytometer. For donor 2 we observe a 2.5 fold increase with the microfluidic device and a 1.5 fold increase with the flow cytometer. Due to unknown factors, not all blood sources responded in the same way to SEB exposure; donor 1 shows a stronger response than donor 2.[ii]

5.4 Discussion

The data from the experimental device shows less resolution between the CD4 and CD14 peaks than with flow cytometry, but similar resolution between the CD14 and

---

[ii]All flow cytometry results shown here were collected at the Wadsworth Center in the New York State Deptartment of Health (NYSDoH) by Renji Song, Joan Peterson-Lane and TJ Ziezeulezicz. Flow cytometry for the CD4, CD14 and J45 cell comparison was performed on a BD FACScan. Flow cytometry for the SEB test on donor 1 was performed on a BD FACSCalibur, and a BD FACScan for donor 2 . Cells were lysed prior to running by temporary dilution in BD PharmLyse™ (BD, Franklin Lakes NJ USA). Ten thousand events were recorded in each case. The same fluorescent antibodies were used with the experimental device and for flow cytometry.

J45 peaks. In the flow cytometry results for the J45 cells there is a significant tail of cells with forward scatter values that are much higher than the peak value, including a high large number of cells (26 of 1834 total cells) that saturated the forward scatter detector. This tail of cells, into high sizes is not seen in the microfluidic device data. It is possible that there are cells or aggregates that have been prevented from entering the microfluidic device by the relatively small gaps and limited depth (20 μm). The difference may also be due to different internal structures in the J45 population that affect light scatter but not "hydrodynamic" size. Other than this effect there is an appealing similarity between the two sets of data despite the very different methods they use for measuring size.

The microfluidic method of size measurement described here is, like forward scatter, somewhat convoluted with cell structure. An exact physical model for the apparent cell size measured by our method (as compared to the size of hard spheres) has not been developed. However, we hypothesize that deformations of an otherwise spherical cell will cause it to appear smaller. The sizes measured here for lymphocytes and monocytes fit with conventional size information, so by the above hypothesis, it is unlikely that these cells are deforming significantly during the measurement process. Decoupling size and deformability could be done using a fixative agent like paraformaldehyde and should be investigated in future work.

In our device we measure cell size by lateral displacement. Other work has shown that by rearranging the post arrays and the exit channels, cells of a certain size range can be collected after passing through the array [47]. Thus our device is capable of passive rare cell collection, provided the rare cells of interest have an abnormal size. In the future other methods of microfluidic cell separation and detection could be integrated to provide enhanced enrichment and separation in a portable, disposable or wearable device. Such a device could provide early detection of certain cancers or immune system responses.

The device described here currently handles thousands of cells per second, the vast majority being red blood cells, with, on average, one lymphocyte per second. The data was obtained by manually inspecting recorded video. Clearly, more advanced image analysis and optics allowing for multicolor labeling would greatly enhance the device throughput and cell identification capabilities.

The microfluidic method used here has been used by others to separate cells in blood [47,67,68]. But none of this other work has shown nearly this level of resolution. Still others [54,69,70] have demonstrated microfluidic particle separation with a related method called pinched flow fractionation. However, our method is potentially advantageous because it is bi-modal and deterministic which allows for more precise control of the particle sizes being separated compared with pinched flow fractionation.

5.5   Summary

Microfluidic flow cytometers currently analyze far fewer parameters than conventional flow cytometry or fluorescence activated cell sorting (FACS) [71,72,66] in order to minimize cost and complexity. There is a need for microfluidic devices that analyze more and or new cell parameters with compact and minimal means. We have demonstrated a new and explicitly microfluidic parameter, "hydrodynamic" cell size, and compare it to forward scatter in conventional flow cytometry. The hydrodynamic size of cells is determined by the degree of lateral displacement experienced while traveling through a 1.2-mm-wide non-clogging array of micro-fabricated obstacles. We show comparable size resolution between the microfluidic device and forward scatter in conventional flow cytometry, and without the need to lyse red blood cells. We use the device to differentiate healthy lymphocytes from "malignant-like" lymphocytes by size alone, and we use the device to detect increased numbers of activated lymphocytes in blood as a result of exposure to staphylococcal enterotoxin B (SEB), a potential bioterror

agent. Together the results demonstrate a microfluidic device that performs some of the measurement and separation tasks of a flow cytometer but at a potentially lower cost and level of complexity.